Predictive Diagnosis of Alzheimer's Disease using Diffusion MRI

by

Syeda Maryam

A thesis
presented to the University of Waterloo
in fulfillment of the
thesis requirement for the degree of
Master of Applied Science
in
Electrical and Computer Engineering

Waterloo, Ontario, Canada, 2016

I hereby declare that I am the sole author of this thesis. This is a true copy of the thesis, including any required final revisions, as accepted by my examiners.

I understand that my thesis may be made electronically available to the public.

Abstract

Age-related neurodegenerative diseases, including Alzheimer's Disease (AD), are an increasing cause of concern for the world's ageing population. The current consensus in the research community is that the main setbacks in the treatment of AD include the inability to diagnose it in its early stages and the lack of accurate stratification techniques for the prodromal stages of the disease and normal control (NC) subject groups. Numerous studies show that AD causes damage to the white matter microstructure in the brain. Commonly used techniques for diagnosing this disease include, neuropsychological assessments, genetics, proteomics, and image-based analysis. However, unlike these techniques, recent advances in Diffusion Magnetic Resonance Imaging (dMRI) analysis posits its sensitivity to the microstructural organization of cerebral white matter, and hence its applicability for early diagnosis of AD. Since tissue damage is reflected in the pattern of water diffusion in neural fibre structures, dMRI can be used to track disease-related changes in the brain. Contemporary dMRI approaches are broadly classified as being either region-based or tract-based. This thesis draws on the strengths of both these approaches by proposing an original extension of region-based methods to the simultaneous analysis of multiple brain regions. A predefined set of features is derived from dMRI data and used to compute the probabilistic distances between different brain regions. The resulting statistical associations can be modelled as an undirected and fully-connected graph encoding a unique brain connectivity pattern. Subsequently, the characteristics of this graph are used for the stratification of AD and NC subjects. Although the current work focuses on AD and NC subject populations, the perfect separability achieved between the two groups suggests the suitability of the technique for separating NC, AD, in addition to subjects in the prodromal stage of the disease, i.e., mild cognitive impairment (MCI).

Acknowledgements

I begin by praising God, the Creator and Sustainer of all the worlds.

First and foremost, I would like to sincerely thank my supervisor, Professor Oleg Michailovich, for giving me the opportunity to pursue MASc at the University of Waterloo. I am grateful to him for his continuous support, guidance, and encouragement throughout the course of my degree. I have gained much from working with him for the past two years and hope to carry it forward in the future.

To Côme, Daniel, José, Laura, Ming, the rest of the Waterloo crowd, and yes, even the elusive James Zachary, thank you for the laughter, the lunch breaks and everything in between. To say you made my lab experience enjoyable would be an understatement. I will cherish those memories for years to come. A special shout-out to all my friends back home. We may be halfway across the world from each other, but you will always be a source of comfort for me no matter where I am.

A very special thank you to the man in my life, Talha. Thank you for waiting and for your love and support over the past year, not to mention all the help with LaTeX and the thesis writing! Without you, I'm not sure I'd have started. To my new family, Talha's mom and dad, thank you for your kindness and support throughout this time. It meant a lot to me.

Last but most importantly, a huge thank you to the family for being my shelter in the storm. Nani, Nana, Ammi, Abbu, Hafsa, and Momina, thank you for believing in me, for rooting for me from the very beginning. Thank you Mamu for being a constant source of inspiration in my life. You and Abbu were my first teachers. This thesis wouldn't have been written if it weren't for you all.

Dedication

For the family, always and forever.
Without you, I'd never have made it.

Table of Contents

List of Figures

List of Tables

Chapter 1

Introduction

Medical imaging, a set of techniques used to capture visual information of internal body structures without surgical intervention, has made rapid progress since its advent in the late 1800s. From the first medical use of X-rays [5] to mapping the human connectome with magnetic resonance imaging [6], much work has been done to develop imaging technologies that are more precise, efficient and accessible to clinicians. Research in medical imaging is driven by two main purposes: first, to acquire diagnostic images to detect disease pathology and assess the effect of treatment, and second, to explore the functionality of internal tissue and organ structures in the body in response to external stimuli.

The choice of a particular image modality is governed by the desired objective, and often involves a trade-off in terms of level of invasiveness, the image resolution, and the signal-to-noise ratio (SNR). For instance, diagnostic ultrasound, an inexpensive and non-invasive imaging modality, is typically used for the assessment of cardiac function and blood perfusion in real time. Alternatively, X-ray imaging provides better representation of anatomical structures and improved SNR, but has the disadvantage of using ionizing radiation and, consequently, cannot be performed frequently. In contrast, Magnetic Resonance Imaging (MRI), a safer and non-ionizing tomographic imaging technique, uses electromagnetic radiation of the radio frequency (RF) spectrum to acquire anatomical and functional information from the body. Since its inception in the 1970s, MRI has rapidly evolved in terms of both hardware and software design, as well as new physical principles, to become the gold standard of modern medical imaging. There are multiple variants of MRI that differ with regard to the data acquisition protocol used and the type of information captured. For example, functional MRI (fMRI) sensitizes the MR signal to blood oxygenation levels in order to monitor the metabolic functioning of the cerebral matter. However, the development of diffusion MRI (dMRI) for quantitative analysis of the random

motion of water molecules has dramatically increased our understanding of microstructural organization and cellular integrity of biological tissue.

In this chapter, the use of MRI-based methods for diagnostic imaging of the brain is highlighted, followed by a brief description of the main contributions presented in this work and an overview of the thesis outline.

1.1 MRI-based Methods for Brain Imaging

The human brain is a highly complex organ that determines a person's thoughts, sensory perceptions and actions. Research has proven that the functional and anatomical connectivity of the brain contains the answers to many prevailing medical questions. The development of MRI techniques has rendered doctors and researchers capable of studying the brain's structure and functionality in a non-invasive manner. MRI offers superior image contrast and spatial resolution in addition to employing non-ionizing radio frequency fields for brain imaging. These favourable characteristics of MRI have made it the method of choice for diagnostic imaging of the brain in both the structural and functional domains [7] [8]. Thus, for example, structural MRI (sMRI) focuses on delineating cerebral cytoarchitecture and anatomy, while fMRI monitors blood perfusion in the brain in response to external stimuli.

Diffusion MRI has garnered much interest from the medical and research communities in recent years. This is because the white matter of the brain, which is composed of neural fibre tracts and accounts for nearly half the brain mass, appears homogeneous in conventional MRI scans [9], making standard MRI an inadequate choice for studying its anatomical organization. However, dMRI quantifies the random thermal motion of water molecules in tissue structures on the micron-scale, enabling the mapping of the fibre tracts in the brain. Particularly, since white matter is known to be implicated in a number of neurological disorders, dMRI can be used for diagnosis of white matter pathology. Consequently, in this thesis, we focus primarily on diffusion MRI and its applications to diagnostic brain imaging.

1.2 Main Contribution

A significant and increasing cause of concern for the world's population is age-related neurodegenerative pathologies, including Alzheimer's Disease (AD). AD is typically characterized by increased forgetfulness, a steady decline in cognitive functioning, and the

inability to perform daily activities. AD affects more than 48 million people worldwide, and half a million Canadians according to the Canadian Mental Health Association. The risk of developing Alzheimer's Disease increases with age, affecting 1 in 11 people over 65 years of age, and 1 in 3 people over the age of 85 [10].

Treatment options for AD are limited largely due to the inability to diagnose the disease in its early stages. Currently, a combination of neuropsychological assessments, genetics, proteomics, and image-based analysis is employed for its diagnosis. Unfortunately, current clinical trends are such that by the time AD is detected, there has already been significant, irreversible brain atrophy in both the gray and white matter [11] [12]. Mild cognitive impairment (MCI), which is widely regarded as a transitional phase between healthy aging and AD, has been the focus of much attention for researchers and medical doctors alike. As it is a known prodromal stage of AD, MCI is regarded as a crucial phase for therapeutic intervention. The past decade has witnessed numerous studies postulating the applicability of dMRI for probing the structural integrity of the white matter for clinical diagnosis of neurological disorders, including AD, Multiple Sclerosis, and epilepsy [13] [14] [15] [16] [17]. The success of this technique can be attributed to its sensitivity to the microstructural properties of cerebral white matter and its ability to delineate complex neural architecture that would otherwise go undetected with conventional MRI. Since disease-related tissue damage is reflected in the pattern of the Brownian motion of water molecules through neural structures, dMRI is well-suited for extracting diagnostic biomarkers from diseased brains.

The fundamental objective of this thesis is the predictive diagnosis of Alzheimer's Disease using information gleaned from diffusion MRI. Specifically, we have developed a conceptually novel scheme to extract diagnostic markers from commonly-available dMRI protocols that can be used for the stratification of AD and NC subject groups. In this work, a predefined set of features derived from diffusion data is used to compute the probabilistic distances between different brain regions. These are then employed as the weights of an undirected and fully-connected graph that encodes the brain connectivity pattern. Subsequently, the characteristics of this graph serve as diagnostic markers to identify AD populations.

The proposed method is characterized by two distinctive features. First, we demonstrate how to adapt diffusion markers usually obtained from sophisticated dMRI acquisition schemes to simpler and clinically-feasible protocols that have already been used to accrue large amounts of study data. Thus, we underscore the usefulness of existing diffusion imaging data for extracting relevant information about the structural integrity of white matter and the development of diagnostic biomarkers. Second, as diffusion imaging analyses may be broadly categorized as region-based, where multiple brain regions are assessed

independently, or tract-based, which reconstruct fibre tracts to investigate brain connectivity, we propose an original extension of region-based approaches to the simultaneous delineation of multiple brain regions, thereby drawing upon the advantages of both approaches. It should be noted that as the proposed method achieves perfect separability between NC and AD groups with considerable margin, the technique holds great promise for fine-grained stratification of NC, AD and MCI populations.

1.3 Outline

The remainder of the thesis is organized as follows:

- Chapter 2 provides a description of the basic principles and concepts underlying diffusion MRI. The effect of the white matter microstructure on diffusion MR signals is also briefly touched upon.
- In Chapter 3, a taxonomy of prevalent, state-of-the-art dMRI imaging techniques and their corresponding acquisition protocols is presented. The taxonomy serves as a comprehensive overview of the diffusion MRI spectrum and establishes the need for analytical methods to exploit information available from simple dMRI protocols.
- The main contribution of the thesis, and the results obtained therefrom are presented in Chapter 4. Specifically, we present the necessary mathematical formulation for the generalization of diffusion metrics usually procured from complex dMRI protocols to simpler acquisition schemes and provide details on how to formulate and apply probabilistically-weighted graphs for clinical diagnosis of AD. The results demonstrate the applicability of the proposed method for clinical diagnosis of Alzheimer's Disease by providing a promising stratification technique for the AD and NC groups.
- The thesis is concluded in Chapter 5 with a summary of the main contributions depicted in this work, and its potential implications for fine-grained stratification of NC, AD and MCI subject groups in the future.

Chapter 2

Principles of Diffusion MRI

MRI is regarded as the modality of choice for diagnostic brain imaging in the clinical setting. It exploits the fact that water accounts for nearly 70% of the human body to generate high-quality images of the underlying anatomical structures. However, the inability of conventional MRI scans to satisfactorily delineate fibre tracts in the brain white matter has prompted the use of diffusion MRI for clinical applications.

The following section provides a brief introduction to the physical principles upon which MRI is based, followed by a description of diffusion MRI and its relevance in diagnosing neurological disorders.

2.1 Magnetic Resonance Imaging

The human body is comprised largely of water and fat, and therefore, contains an abundance of hydrogen nuclei. Each nuclei possesses a magnetic dipole and is spinning, or *precessing* about its axis. This phenomenon is called a *nuclear spin system*. Broadly speaking, the system can have two fundamental energy states (excited and relaxed), and the absorption and emission of RF energy causes it to oscillate between the two. This inherent property of the nuclear spins is the basis of MRI.

A typical MRI scanner is composed of a constant-field magnet, RF coils and a magnetic field gradient system [18]. The imaging magnet produces a strong homogeneous static magnetic field, B_0, with a field strength in the range of 1.5T–3T directed along the scanner bore. When the patient enters the MRI machine, a substantial proportion of the hydrogen nuclei in her or his body are aligned in the direction of the B_0 field, and precessing about

their axes in the lower energy state mentioned earlier. The precession frequency, w_0, of each spin, also called the Larmour frequency, is dependent on the strength of the magnetic field and the nuclei themselves and is described by the Larmour equation as

$$w_0 = \gamma B_0, \tag{2.1}$$

where γ is the gyromagnetic ratio, a physical constant that is specific to the type of nuclei measured in units of rad/s/T.

The nuclear spin system can be excited to the higher energy level from its steady state by the application of an RF pulse at the Larmour frequency, which generates a time-varying magnetic field, $B_1(t)$, perpendicular to B_0. The effect is to rotate the bulk magnetization about B_1 and away from B_0, thus creating a *forced precession*. Once the RF field is switched off, the nuclei return to their original state through a process of *relaxation*. The resulting electromagnetic radiation that is emitted from coherently precessing spins induces an equivalent exponential signal decay in the MR receiver coils from which the MRI image can be reconstructed. This phenomenon is termed nuclear magnetic resonance (NMR).

In the absence of any additional magnetic fields, the Larmour frequency, and hence the electromagnetic signal decay, would be the same for all hydrogen nuclei, irrespective of their position in the body, preventing us from obtaining any useful information about internal tissue structures. Therefore, the main B_0 field is augmented with a spatially-varying magnetic field produced by the scanner's gradient magnets for *spatial encoding*. The gradient magnets can linearly vary the main magnetic field along one of three orthogonal directions and are hence often called $G_x(t)$, $G_y(t)$ and $G_z(t)$ [1]. This essentially makes the Larmour frequency of each spin position dependent, enabling us to discriminate between the signals coming from different positions of the body. The NMR phenomenon, coupled with the aforementioned spatial encoding technique, forms the foundation of MRI[18].

The observable image contrast in a typical MRI scan is governed by multiple factors, including the underlying tissue density and relaxation times of the bulk vector magnetization after the absorption of RF energy. Measuring the signal decay of different projections of this vector can provide us with various decay constants with the representative images reflecting the relative distribution of the relaxation times. For instance, the T1 decay constant is determined by the time taken for the spin system to realign itself with the B_0 field and accounts for spin-lattice interaction, while T2 depends on the decay of the precessing part of the magnetization [1] and accounts for the spin-spin interaction. Consequently, both contrasts tend to complement each other: tissues with high fat content appear bright and water-filled regions show up dark in a T1 scan, while the converse is true for T2-weighted images. It should be noted that T1 and T2 are the most prevalent contrasts among others.

2.1.1 MRI Imaging Sequences

The pixel values of an MRI image depend on the signal strength induced in the receiver coils, which in turn is determined by the phase coherence of the hydrogen spins undergoing relaxation. Minor variations in the B_0 field can lead to small irregularities in the frequencies of precessing spins (according to Equation 2.1). This in turn causes spins to lose their phase coherence, resulting in the electromagnetic MR signal decaying much more rapidly than it would if only governed by T2 decay [1]. To ensure signal loss detected by the MR receiver coils is only due to T2 decay and not spin dephasing, it is a standard practice to use another refocusing RF pulse (known as a 180° pulse), which is applied a time τ after the application of the first excitation pulse (90° pulse) to remove phase incoherence. First introduced by Erwin Hahn [19], this allows the slower precessing spins to "catch up" with the faster ones, until they are all back in phase at a time 2τ after the initial RF pulse, called the spin echo. The aforementioned protocol is termed a spin echo pulse sequence. Imaging sequences that do not employ refocusing pulses are called gradient echo sequences [1].

Spin echo sequences are characterized by two parameters: the echo time (TE) and the repetition time (TR). TE = 2τ is defined as the time between the application of the first 90° RF pulse that induces spin excitation and the occurrence of the spin echo at which the signal is detected by the scanner (see Figure 2.1). The 180° refocusing RF pulse is generally applied at a time TE/2 = τ. TR is the time between two consecutive RF excitation pulses.

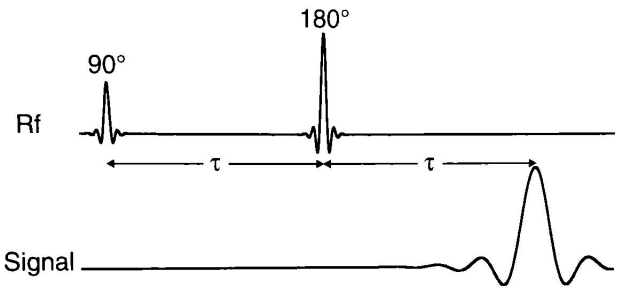

Figure 2.1: Hahn's spin echo pulse sequence. A 90° RF pulse is applied to induce spin excitation, followed by a 180° refocusing pulse applied at a time τ to remove phase incoherence of the spins. The spin echo is detected by the MR receiver coils at a time 2τ after the initial RF pulse. Credit: [1].

2.2 Diffusion MRI

According to Fick's law, diffusion is described as the net motion of particles from a region of relatively higher concentration to one of lower concentration. However, on the molecular level, particles continue to exhibit thermal motion at temperatures above zero degrees kelvin, even in the absence of a concentration gradient [1]. This gives rise to the process of self-diffusion or Brownian motion which is different from bulk transport mechanisms (e.g., convection or dispersion). Since diffusive mixing arises from collisions between molecules and atoms, it is influenced not only by the size of the diffusing molecules but also the microstructural features of the surroundings and hence, it can serve as a sensitive measure for probing the characteristics of biological tissue.

The trajectory followed by a self-diffusing molecule in three-dimensional space is a random walk, making it impossible to predict where a single particle will diffuse to in a given time interval. However, in the early 20th century, Albert Einstein showed that the diffusion behaviour for a large number of freely-moving particles could be characterised as

$$\langle r^2 \rangle = 6Dt, \tag{2.2}$$

where $\langle r^2 \rangle$, the mean-squared displacement undergone by the particles is directly proportional to the diffusion time t, and the self-diffusion coefficient, D.

If the probability of displacing a given distance from the origin is equal in all directions, the molecules are said to exhibit isotropic motion. Equation 2.2 is derived based on the assumption that this isotropic diffusion can be characterized by a Gaussian function, and encapsulates the variance of the distribution. Figure 2.2 depicts the Gaussian distributions of displacements in one, two, and three dimensions, along with their respective standard deviations as functions of time.

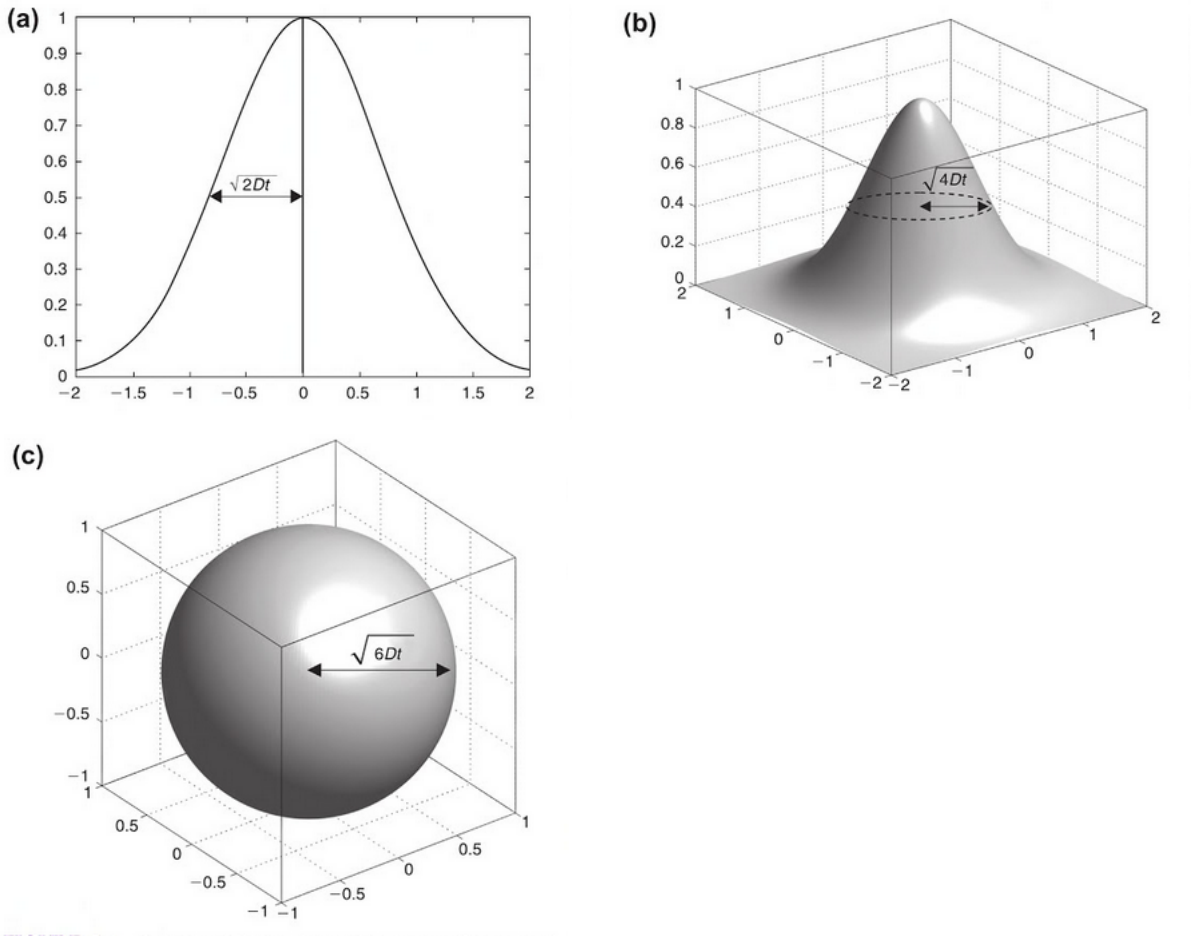

Figure 2.2: Gaussian diffusion as characterized in (a) one, (b) two, and (c) three dimensions. The diffusion probability distribution in an isotropic medium (i.e., probability of diffusion is uniform in all directions) has a spherical shape in three dimensions. Credit: [1].

2.2.1 Adding Diffusion Weighting to MRI Imaging Sequences

In 1950, Hahn proposed that the spin echo MR signal (Figure 2.1) could be made sensitive to the thermal motion of water molecules [19], which was expanded upon by Carr and Purcell in 1954 [20]. They noted that since the precessional frequency of a molecule depended on the strength of the local magnetic field (refer to Equation 2.1), the application of a linearly varying magnetic field gradient across the specimen would cause molecules to

experience varying magnetic fields at different locations, thereby leading spins at different positions to precess at different frequencies. This would cause particles to accrue spatially-dependent phase shifts determined by their respective locations. The net phase shift of the MR signal would then rely on the diffusive motion of the molecular ensemble, making the spin echo signal susceptive to diffusion. The superimposition of such diffusion-encoding gradients on the standard MRI pulse sequence is termed diffusion weighting, and lies at the heart of dMRI.

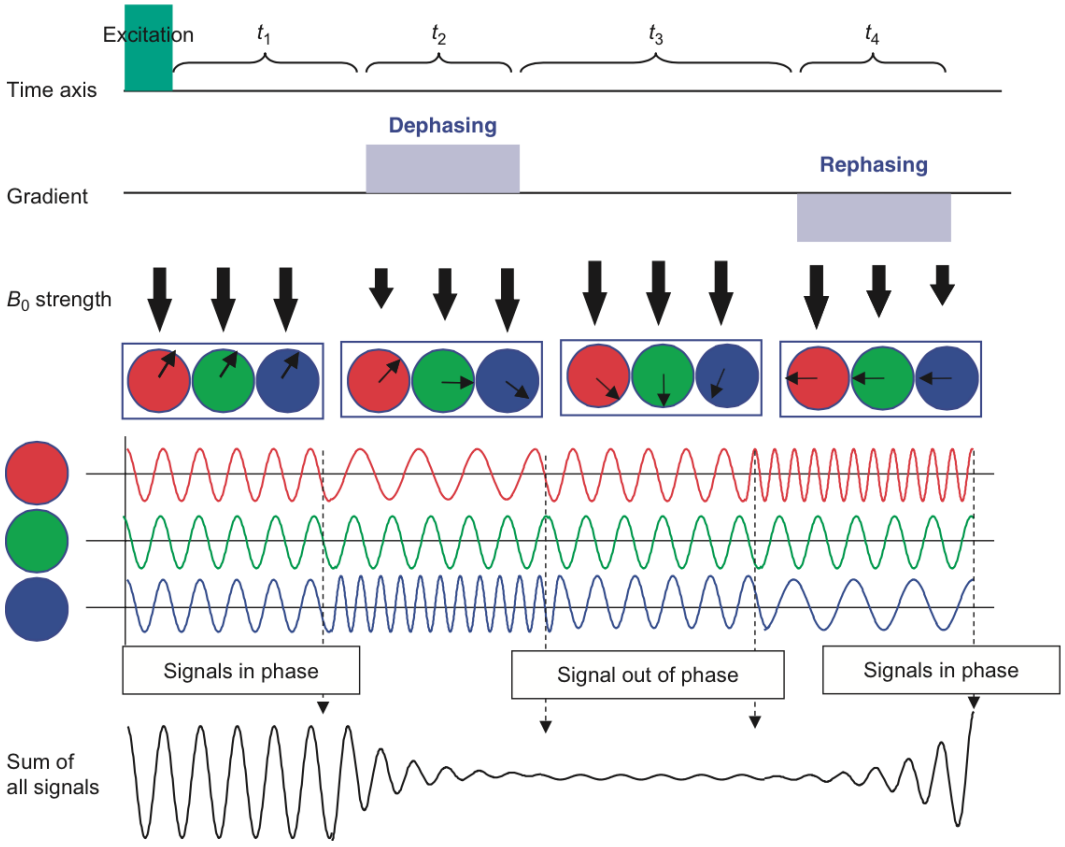

Figure 2.3: Dephasing and rephasing gradient pulses for diffusion encoding. Credit: [2].

Figure 2.3 demonstrates the effect of applying diffusion-encoding gradients on the resulting MR signal strength. After the RF excitation pulse, the spins are in phase, leading to an increase in the MR signal detected by the receiver coils. The dephasing gradient pulse at t_2 introduces a linearly varying phase shift across the volume. Specifically, spins

to the left (shown in red) are subjected to a weaker magnetic field, while spins on the right (shown in blue) experience a stronger field. Consequently, spins on the left precess at slower frequencies than the ones on the right, accruing spatially dependent phase shifts for the duration of t_3. Once the dephasing pulse has been turned off, the spins revert to their original precessional frequencies but are no longer in phase. The phase incoherence of the spins causes the MR signal output to be attenuated. The rephasing pulse at t_4 seeks to remove the dephasing by applying a linearly varying magnetic field in the reverse direction to the volume. If there has been no net molecular motion between the two gradient pulses, the phase shift introduced at t_2 will be cancelled out by the rephasing pulse, and the spins will once again be in phase, leading to an increase in the signal strength. However, if the molecules have undergone diffusion-induced displacement, the phase shift will not be entirely removed, which will be reflected in the strength of the MR signal. The principle thus described forms the basis for the Pulsed Gradient Spin Echo (PGSE) sequence, first proposed by Stejskal and Tanner in 1965, and described in detail in the following section.

2.2.2 The Pulsed Gradient Spin Echo Sequence

It was not until the advancements put forward by Stejskal and Tanner in 1965 that modern-day diffusion measurements in MRI became viable. In their seminal work, they introduced a new MR acquisition protocol, the pulsed gradient spin echo sequence (PGSE) onto which diffusion-encoding gradient fields could be superimposed to finish the work started by Carr and Purcell [21]. Instead of a constant magnetic field gradient, they proposed using dual "narrow pulse" gradients of a shorter duration, i.e., a pair of dephasing and rephasing short gradient pulses were employed to sensitize the MR signal to molecular displacements. The *narrow pulse approximation* stipulated that molecular diffusion for the duration of the gradient pulses could be disregarded.

Figure 2.4 depicts a schematic of the PGSE sequence. The first gradient (the dephasing gradient), applied after the 90° RF pulse, tags nuclear spins with a positive phase, the strength of which depends on their position in the medium. In the one-dimensional case, the resulting net phase shift of the molecular ensemble can be expressed by

$$\phi_1 = -qx_1,$$

where the variable $q = \gamma\delta G$ summarizes the PGSE experimental parameters, δ denoting the duration of the pulse gradient, G the strength of the magnetic gradient and x_1 the location of the spin under consideration. Similarly, the second pulse gradient applied after a *diffusion time*, Δ, induces a net phase change in a particle positioned at x_2 given by

$$\phi_2 = -qx_2.$$

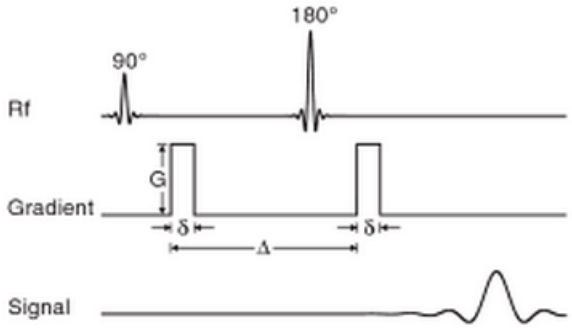

Figure 2.4: Stejskal and Tanner's PGSE sequence. Credit: [1].

Since the second gradient lobe occurs after the 180° RF pulse, it introduces a phase change that is equivalent but reversed in direction to the first. Hence, the cumulative phase shift can be represented as

$$\phi_2 - \phi_1 = -q(x_2 - x_1).$$

If spins remain stationary throughout the sequence, $\phi_2 - \phi_1$ will be zero since the phase shift triggered by the first pulse gradient will be entirely cancelled out by the second. However, if spins diffuse throughout the imaging specimen, the phase difference will not cancel out and the resulting signal will be attenuated due to the phase incoherence of the spins. This signal decay can be attributed to the phase dispersion or self-diffusion of the spin system.

Since the orientation of the diffusion-encoding pulses characterizes the diffusion profile along that direction, it is necessary to apply diffusion gradients in a multitude of directions to gain a more complete representation of molecular diffusion. In such a case, both $\mathbf{G}$ and $\mathbf{x}$ will be three-dimensional vectors, and hence so will $\mathbf{q}$. It follows that the space of all possible gradient directions is known as the $\mathbf{q}$-space. The acquisition parameters of the PGSE sequence, including the gyromagnetic ratio γ, the duration δ and strength $|\mathbf{G}|$ of the magnetic field gradients, and the time Δ between the application of the two opposing pulses can be summed up in a single variable known as the b-value, which is related to $\mathbf{q}$ by the following equation

$$b = ||\mathbf{q}||^2(\Delta - \delta/3). \tag{2.3}$$

The MR signal attenuation is measured with respect to a signal acquired in the absence of diffusion-encoding gradients. Hence, a single diffusion measurement involves acquiring a signal with no diffusion weighting, i.e., $b = 0$, and one with non-zero diffusion weighting in the direction along which diffusion is to be measured. Generally, the attenuative effect

of diffusion is described in terms of the ADC as shown

$$\frac{S}{S_0} = e^{-b \cdot ADC}, \tag{2.4}$$

where S is the diffusion signal acquired at a high b-value, S_0 is the signal obtained without diffusion weighting, and ADC is the apparent diffusion coefficient. The ADC can be formally defined as

$$ADC = -\frac{\log(S/S_0)}{b}. \tag{2.5}$$

Consequently, the ADC in each voxel of the imaged volume can be estimated using Equation 2.5.

The Stejskal-Tanner formalism has led to the development of a variety of tools and protocols that fall under the umbrella of diffusion MRI. As water molecules will diffuse at different rates in different brain regions depending on their constituent compartments and cellular concentrations, diffusion MRI is particularly useful for probing the diffusion process, and thereby the underlying the structural integrity of the white matter of the central nervous system (CNS) at a microscopic scale.

2.2.3 q-Space Acquisition

In the PGSE sequence, the effect of diffusion-encoding is represented by means of a 3D vector $\mathbf{q}$ in the $\mathbf{q}$-space, which is oriented in the direction of diffusion and proportional to the product of the gradient strength and pulse length. Therefore, the application of a PGSE sequence samples a 3D point in the $\mathbf{q}$-space, resulting in one diffusion-weighted image (DWI). In other words, in brain imaging, a single PGSE sequence amounts to a full cranial scan. Sampling the entirety of the $\mathbf{q}$-space entails repeated applications of the PGSE sequence at multiple $\mathbf{q}$ values, i.e., gradient strengths and orientations, providing us with a myriad of DWIs, each of which corresponds to a distinct diffusion weighting. Consequently, each voxel in the imaged volume will have a $\mathbf{q}$-space signal with many samples acquired at multiple directions. The signal can be shown to be related to the displacement distribution through the Fourier Transform (FT).

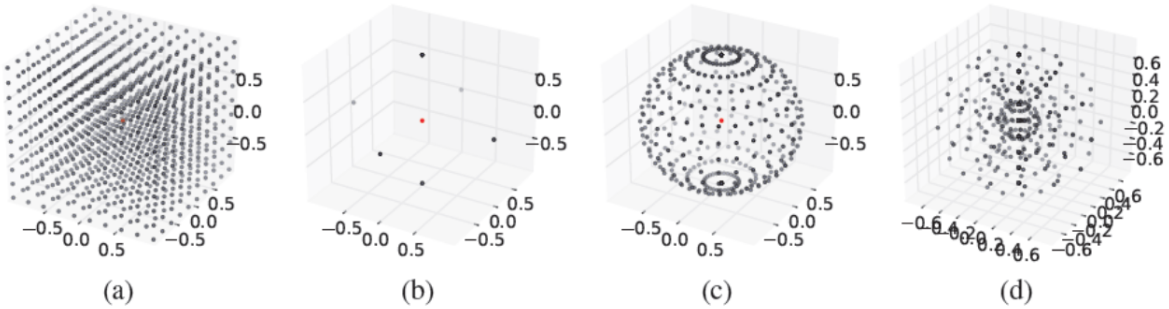

Figure 2.5: Sampling schemes for dMRI. (a) Cartesian sampling of the **q**-space, (b), (c) single-shell sampling with small and large number of measurements, and (d) Multi-Shell Diffusion Imaging. The **q**-space origin is featured in red. Credit: [3].

dMRI methods differ depending on the specific **q**-space sampling scheme employed for DWI acquisition. Sampling schemes may be single-shell, multi-shell or Cartesian. In single-shell diffusion imaging, **q**-space acquisition is performed at a single b-value or spherical shell (magnitude of **q** is fixed) at different diffusion-encoding directions. In contrast, Multi-Shell Diffusion Imaging (MSDI) samples the **q**-space at more than one b-value (multiple spherical shells) and multiple gradient directions. Sampling the **q**-space on a Cartesian grid is currently infeasible due to the long acquisition times it would necessitate [3].

The following section highlights the applicability of diffusion MRI for discriminating the white matter of the brain and diagnosing neurodegenerative disorders.

2.2.4 Diffusion MRI in Neurological Disorders

The white matter of the brain is highly ordered due to the underlying axonal architecture. Neural tracts in the central nervous system (CNS) are typically composed of bundles of axons surrounded by myelin sheaths. The tracts appear to be "white" because of the myelin, which serves as an electrical insulator between the fibres. Due to the highly oriented nature of white matter, water molecules tend to diffuse along the length of fibre tracts, with movement being largely restricted in the orthogonal directions. Preferential diffusion in one direction over another is termed anisotropic and is characteristic of tightly-packed directional fibrous structures, such as the corpus callosum. When molecular motion is unrestricted and equally likely in all directions, as is the case in the cerebrospinal fluid

(CSF), diffusion is said to be isotropic. Recent studies have shown that the myelin coating around nerve fibres is conducive to their integrity [22], indicating that water diffusion in myelinated axons is found to be more anisotropic than in demyelinated ones. This is termed the *myelin hypothesis* [23].

Conventional MRI scans are unable to discern this complex microstructure owing to the fibre diameters being roughly on the order of 1μm–30μm [24]. Diffusion MRI has the ability to gauge molecular displacements in the 5μm–10μm range, and since these displacements depend on interactions with the underlying microstructure, it can be used to visualize the neuroanatomy of the cerebral tissue despite the image resolution being several orders of magnitude lower.

Diffusion MRI can be used for the diagnosis of white matter pathology. A number of neurological disorders and diseases lead to alteration of the white matter tissue and loss of structural integrity. Demyelination and axonal degeneration are the two main causes of morphological changes in the white matter [1]. Thus, for example, Multiple Sclerosis (MS) is one such demyelinating disease that affects myelin sheaths in the CNS. Degradation of the axonal architecture can be instigated by a range of disorders, including MS, motor neuron disease and Alzheimer's Disease [1]. In such cases, dMRI is commonly preferred as the method of choice for non-invasively imaging the cerebral tissue microstructure, as it quantifies the demyelination and axonal loss in terms of diffusion measurements, which would otherwise go undetected with conventional MRI. In particular, there are clinical applications, such as in the diagnosis of acute ischemia, in which a T1 or T2-weighted scan of the brain appears to be normal, while a dMRI scan shows a reduction in the displacement of water molecules per unit time [1] [25]. dMRI-based clinical diagnosis holds great promise for a diverse range of neurological disorders and conditions, as demonstrated in a large number of clinical studies involving Parkinson's Disease, AD, MS, and Huntington's Disease to name a few [26].

Chapter 3

Methods and Models of Diffusion MRI

There are many variants of diffusion MRI that differ with regard to the modeling assumptions employed to represent the diffusion profile. For example, Diffusion Tensor Imaging (DTI), the simplest and most commonly used dMRI technique, ascribes a unimodal Gaussian model to water diffusion at each voxel [27]. It requires a minimal number of measurements but is unable to satisfactorily resolve crossing fibre regions in the brain. Alternatively, multi-compartment models, such as the "ball and stick" proposed by Behren et al. [28], more accurately depict the diffusion process by characterising it as a weighted combination of isotropic (ball) and anisotropic (stick) terms. More accurate models are suggested by Diffusion Spectrum Imaging (DSI) and Q-Ball Imaging (QBI), albeit at the cost of a substantial increase in the number of measurements. Such techniques their attempt to approximate the diffusion probability distribution directly without explicitly attributing a geometric model to the diffusion signal.

It is important to realize that each approach, whether it be model-based or non-parametric i.e., "model-free", places its own stringent requirements on the data acquisition protocol needed to characterize the diffusion signal. For instance, the DTI model can be fit with as few as 6 measurements (although it is common to acquire more to counteract the effect of noise via averaging). More commonly, most DTI regimes acquire 20-30 DWIs along gradient directions uniformly distributed on a single spherical shell (i.e., constant b-value), indicating a relatively short acquisition time (under 15 minutes). In contrast, methods that provide analytical representations of the diffusion signal such as Mean Apparent Propagator (MAP) MRI typically depend on data acquired on a very large set of

q-vectors (greater than 500) at multiple b-values, leading to scan times approximately an hour long if not more [29].

Clinical scan durations are a critical factor when designing MR experiments. Most patients suffering from neurological or psychiatric conditions are unable to withstand scan times longer than 15 minutes [30]. Hence, standard clinical protocols generally do not make allowances for scan times of 30 minutes or higher, rendering modern dMRI techniques that rely on more complex data-acquisition schemes clinically infeasible.

This chapter presents an abbreviated taxonomy of parametric and non-parametric diffusion MRI methods that have gained traction over the last decade. Details of the techniques, along with their respective data acquisition requirements have been summarised, with particular focus given to DTI as it is the most widely used dMRI protocol today. Before delving into the various approaches, it is instructive to describe some useful quantities that can be approximated from dMRI and utilised for delineating the architectural features of the imaged volume.

3.0.1 Fibre Orientation Distribution Function

A particularly important quantity that reflects the distribution of fibre configurations is the fibre orientation distribution function or fODF. The fODF is essentially a probability distribution defined on the sphere and is used to determine the fraction of fibre populations oriented along each direction within a voxel. If estimated correctly, the fODF would be able to discriminate a range of fibre configurations, including situations wherein fibres vary in orientation along their length (e.g., fanning and bending populations).

3.0.2 Ensemble Average Propagator

The diffusion propagator, $P(\mathbf{x_1}, \mathbf{x_2}, \Delta)$ expresses the probability of a spin undergoing a spatial displacement from an initial location $\mathbf{x_1}$ to a final location $\mathbf{x_2}$ in a diffusion time Δ. Since a local propagator can be assigned to each location or voxel in the image, it is possible to obtain an aggregate measure of molecular diffusion in the specimen, termed the Ensemble Average Propagator (EAP), by integrating over all initial spin positions as shown [21] [31]

$$EAP = P(\mathbf{x}, \mathbf{\Delta}) = \int_{\mathbf{R}^3} \rho(\mathbf{x_1}) P(\mathbf{x_1}, \mathbf{x_2}, \Delta)\, d\mathbf{x_1}, \tag{3.1}$$

where $\mathbf{x} = \mathbf{x_2} - \mathbf{x_1}$ is the displacement incurred and $\rho(\mathbf{x_1})$ quantifies the spin density at $\mathbf{x_1}$. Hence, $P(\mathbf{x}, \mathbf{\Delta})$ describes the total probability of a spin experiencing a displacement $\mathbf{x}$ from all possible spin densities $\rho(\mathbf{x_1})$.

The normalized diffusion signal, $E(\mathbf{q}) = \dfrac{S(\mathbf{q})}{S_0}$, is related to the EAP through the Fourier Transform [21] [31]

$$P(\mathbf{x}, \Delta) = \int_{\mathbf{R}^3} e^{i2\pi\mathbf{q}\cdot\mathbf{x}} E(\mathbf{q})\, d\mathbf{q}, \tag{3.2}$$

where $\cdot$ represents the Euclidean dot product, $\mathbf{q}$ is the wave vector comprising the experimental parameters of the MR experiment, which can now be redefined as $\mathbf{q} = \gamma\delta|\mathbf{G}|\mathbf{u}$, with $\mathbf{u}$ denoting the unit vector of the corresponding diffusion gradient. It should be noted that equation (3.2) assumes that the narrow pulse approximation holds for the specific pulse sequence used for data acquisition, i.e., the magnetic field gradients are of such a short duration that molecular diffusion during this time span can be neglected.

3.0.3 Diffusion Orientation Distribution Function

An additional quantity of interest that can be derived from the EAP is the dODF or ODF. Like the EAP, the ODF is a probability distribution of the diffusion displacement, the difference being that it is defined over the unit sphere. Hence, the ODF indicates the orientation along which diffusion is likely to take place within a voxel. First introduced by Tuch, the ODF can be obtained from the EAP by integrating over the radial component [32]

$$\psi(\mathbf{u}) = \frac{1}{Z} \int_0^\infty P(r\mathbf{u}) r^2 dr, \tag{3.3}$$

where Z is a dimensionless normalization constant, and $P(r\mathbf{u})$ estimated in the direction of $\mathbf{u}$ and expressed in spherical coordinates. Therefore, $\psi(\mathbf{u})$ is simply the radial projection of the ensemble average propagator and is considered a marginal distribution of the EAP. Figure 3.1 depicts the ODFs associated with specific fibre configurations, including parallel and crossing fibre tracts. As can be seen, the normalized version of the dODF and the fODF emphasize the directional characteristics of the fibre distribution.

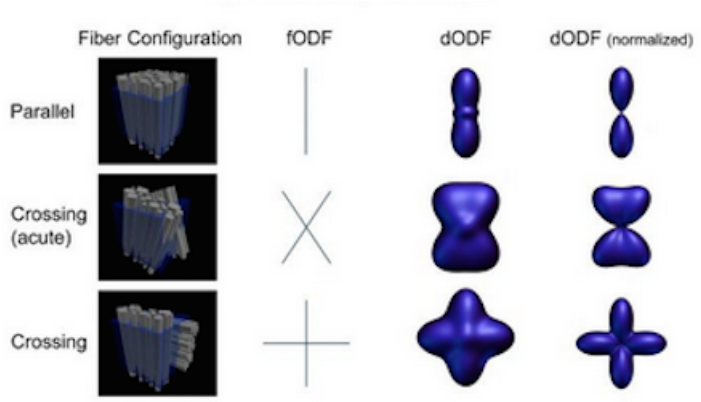

Figure 3.1: Orientation distribution functions corresponding to different white matter configurations. The normalized dODF highlights the directional characteristics of the original dODF. Credit: [1].

Both the MR signal and the EAP are representative of the underlying microstructural environment. Specifically, the ODF is considered to be a blurred version of the fODF [33]. Since the limited image resolution of diffusion MRI prohibits their direct measurement from diffusion data, the goal of most dMRI schemes is to attain an approximate representation instead, enabling the characterization of voxel-averaged diffusion descriptors in the imaged volume. dMRI methods can be broadly categorized as being either model-based or parametric, where an explicit model is employed to represent distinct fibre populations and hence, the diffusion behaviour, or non-parametric, which focus on obtaining a direct representation of the fODF without relying on an exact model.

3.1 Model-Based Approaches

A number of well-established parametric diffusion MRI methods are described in this section, starting with the ubiquitous diffusion tensor model [27].

3.1.1 Diffusion Tensor Imaging

A single value of the apparent diffusion coefficient at each voxel (refer to Equation 2.5) proves to be insufficient in delineating anisotropic tissue structures in the imaged volume. It becomes necessary to employ a model to characterize the diffusion profile of water

molecules in such regions. One of the simplest models that can be used for this purpose is the diffusion tensor, which assumes the diffusion process to be Gaussian. Conceptually, the diffusion tensor can be depicted as an ellipsoid, with its surface expressing the distance a particle will diffuse with equal probability from the origin. Hence, in an anisotropic medium, the tensor resembles an elongated ellipsoid, with its major axis denoting the long axis of the medium, i.e., the direction along which molecular diffusion predominates whereas in an isotropic region, such as the CSF, the diffusion tensor tends to be spherical in shape.

Mathematically, the diffusion tensor is a 3×3 symmetric positive-definite matrix representing the covariances of molecular displacements along the scanner measurement frame axes (x, y and z-axes). The diagonal elements D_{xx}, D_{yy} and D_{zz} depict the diffusivities along the respective axes while the off-diagonal elements indicate the correlations between displacements along those axes [1], for instance, D_{xz} is the covariance between displacements along the x- and z-axes. Hence, the diffusion tensor $\mathbf{D}$ is shown to be

$$\mathbf{D} = \begin{bmatrix} D_{xx} & D_{xy} & D_{xz} \\ D_{yx} & D_{yy} & D_{yz} \\ D_{zx} & D_{zy} & D_{zz} \end{bmatrix}.$$

Diagonalizing $\mathbf{D}$ provides us with its eigensystem so that the principal axes of the ellipsoid are defined by the mutually orthogonal eigenvectors (ϵ_1, ϵ_2, ϵ_3), and scaled with respect to the square root of the eigenvalues ($\lambda_1, \lambda_2, \lambda_3$) which correspond to diffusivites along those axes. Hence, the diffusion tensor is oriented along the principal eigenvector, i.e., the eigenvector related to the largest eigenvalue and represents the orientation of the dominant fibre population in each voxel of the imaged volume. Figure 3.2 demonstrates how a single fibre tract can be modelled using DTI, with the major axis of the ellipsoid oriented along the length of the tract.

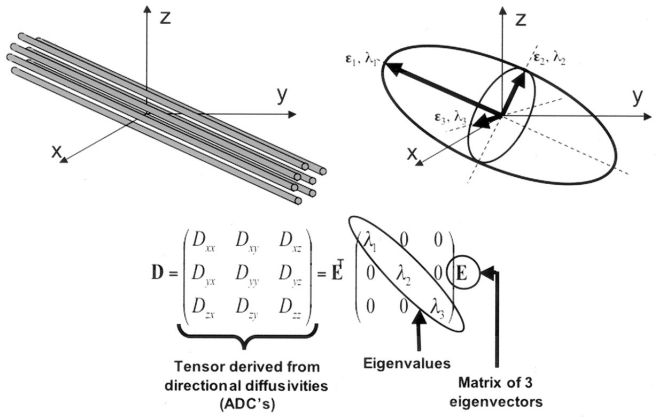

Figure 3.2: Modelling a coherently-oriented fibre tract with the diffusion tensor ellipsoid. The ellipsoid is characterized by the eigensystem of the diffusion tensor, with the principal eigenvector denoting the dominant fibre direction. Credit: [4].

Estimating the Diffusion Tensor

For Gaussian displacement distributions, the Stejskal-Tanner formalism in equation (2.4), can be encapsulated as follows

$$\frac{S}{S_0} = e^{-b\mathbf{u}^T\mathbf{D}\mathbf{u}}, \tag{3.4}$$

where b is the b-value (refer to Equation 2.3), $\mathbf{u}$ is the unit vector of the diffusion-encoding gradient and $\mathbf{D}$ is the diffusion tensor. Since the diffusion tensor is symmetric about the diagonal, there are only six elements to be determined, namely D_{xx}, D_{yy}, D_{zz}, D_{xy}, D_{xz}, and D_{yz} and therefore, a minimum of six diffusion-weighted images [1] are sufficient to fit the tensor. However, to alleviate the effect of noise in the data, it is usual to acquire images along a larger set of diffusion-encoding directions, usually 20-30 gradient orientations distributed uniformly on a unit sphere [3], after which $\mathbf{D}$ can be computed from the log-transformed signals using a least squares estimation routine [1].

[1] Often, a DWI with no diffusion-weighting is also acquired for normalization purposes

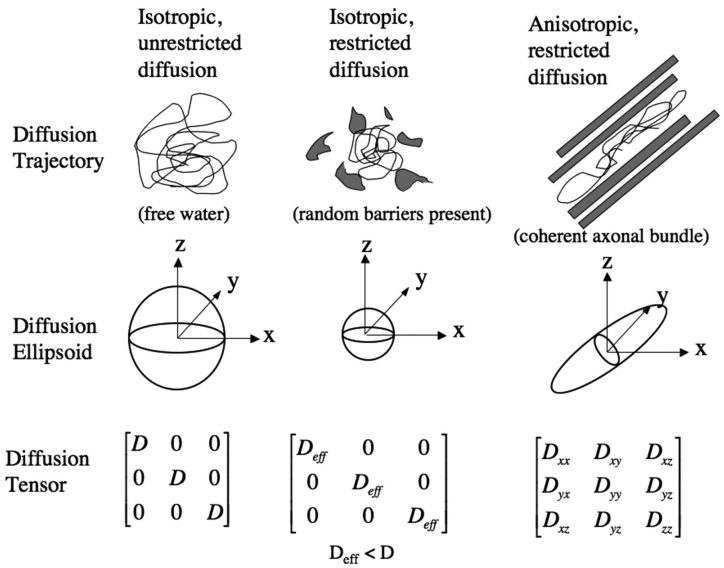

Figure 3.3: Diffusion tensor matrices and ellipsoids corresponding to isotropic and anisotropic diffusion profiles. The diffusion ellipsoid resembles a sphere in isotropic media (e.g., free water), with the diagonal elements of the tensor denoting the diffusion coefficients along the axes. The presence of random barriers in an isotropic medium implies only effective values of D can be measured. For the case of anisotropic diffusion, the diffusion ellipsoid is oriented in the fibre direction. Credit: [4].

Tensor Metrics

The eigenvalues of the diffusion tensor can be manipulated to provide rotationally-invariant metrics within each voxel of the image. The trace, mean diffusivity (MD), fractional anisotropy (FA), relative anisotropy (RA) and volume ratio (VR) are some of the metrics derived from $\mathbf{D}$ that can provide useful information about diffusion anisotropy. The trace is essentially a measure of the diffusivity while mean diffusivity is defined as the average of the tensor eigenvalues. Specifically,

$$\text{Trace} = \lambda_1 + \lambda_2 + \lambda_3, \tag{3.5}$$

$$\text{MD} = \langle \lambda \rangle = \frac{\lambda_1 + \lambda_2 + \lambda_3}{3}. \tag{3.6}$$

The FA is particularly useful for quantifying the diffusion anisotropy within a voxel. If diffusion is isotropic, the tensor eigenvalues tend to be similar and consequently, the FA

values approach 0. Alternatively, in anisotropic regions such as a highly directional fibre population, the diffusion tensor resembles an elongated ellipsoid with one eigenvalue dominating the others, causing FA values to peak closer to 1. The FA is defined as,

$$\mathrm{FA} = \sqrt{\frac{3}{2}} \frac{\sqrt{(\lambda_1 - \langle\lambda\rangle)^2 + (\lambda_2 - \langle\lambda\rangle)^2 + (\lambda_3 - \langle\lambda\rangle)^2}}{\sqrt{\lambda_1^2 + \lambda_2^2 + \lambda_3^2}}. \tag{3.7}$$

Similarly, the RA and VR have been derived to be

$$\mathrm{RA} = \sqrt{\frac{1}{3}} \frac{\sqrt{(\lambda_1 - \langle\lambda\rangle)^2 + (\lambda_2 - \langle\lambda\rangle)^2 + (\lambda_3 - \langle\lambda\rangle)^2}}{\langle\lambda\rangle}, \tag{3.8}$$

$$\mathrm{VR} = \frac{\lambda_1\lambda_2\lambda_3}{\langle\lambda\rangle^3}. \tag{3.9}$$

Finally, it should be noted that the aforestated anisotropy indices do not reflect the shape of the tensor ellipsoid as different combinations of eigenvalues can result in high anisotropy values. To this end, Westin et al. [34] proposed his linearity (C_l) and planarity (C_p) metrics in 1997. These measures allow the quantification of the prolateness and oblateness of the diffusion ellipsoid. Namely,

$$\mathrm{C}_l = \frac{\lambda_1 - \lambda_2}{\lambda_1}, \tag{3.10}$$

$$\mathrm{C}_p = \frac{\lambda_2 - \lambda_3}{\lambda_1}. \tag{3.11}$$

One of the major clinical applications for DTI metrics is the diagnosis of acute ischemic lesions in the CNS where the MD or trace is found to decrease in the acute phase and increase for chronic lesions [35] [36]. Additionally, a recent study on paediatric brain tumour patients found correlations between the MD and tumour grade and cellularity [37]. Since FA estimates how anisotropic the diffusion process is, it can serve as a useful indicator of demyelination in white matter fibre tracts, with studies showing a reduction in FA in brains suffering from myelin loss [38]. It has also been recognized that the FA is significantly reduced in selected white matter regions including the hippocampal white matter, corpus callosum, cingulum and uncincate fasciculus for patients suffering from AD [26]. Furthermore, both FA and MD in the cerebellum and basal ganglia have been utilized for the discrimination of different types of Parkinsonian disorders as outlined in [39] [40] [41].

Acquisition Requirements

The underlying modelling assumptions of DTI entail that it can only determine a single fibre population in each voxel of the imaged volume, and hence fails in areas of crossing fibres. As a result, FA and MD might not serve as accurate diffusion metrics in regions of crossing fibre tracts. Despite this limitation, DTI remains popular in the clinical setting largely due to its clinically feasible acquisition times. This is an important factor to consider when designing MR experiments as shorter acquisition times are well-tolerated by patients and can result in reduced motion artifacts. It is now possible to obtain high quality diffusion tensor MR data with whole-brain coverage at 2.5 mm isotropic resolution and 64 diffusion-encoding directions with a 1.5T scanner in approximately 15 minutes, as described in [30].

3.1.2 Multi-Compartment Models

Multi-compartment models represent brain white matter as a weighted combination of three types of compartments, where each compartment captures a different property of molecular diffusion. Notably, diffusion can be categorized as being restricted in the intra-axonal space, hindered in the extra-axonal space, or isotropically restricted in other cellular structures [42], with the underlying assumption being that there is no molecular exchange between the compartments. Combinations of two or three compartments provide a more coherent picture of the diffusion process in highly-ordered brain tissues and specifically in regions of crossing fibres, which the DTI model is unable to satisfactorily resolve. The general equation for the multi-compartment model is expressed as

$$\begin{aligned} S &= \sum_{i=0}^{3} f_i S_i \\ \sum_{i=1}^{3} f_i &= 1, \quad 0 \leq f_i \leq 1, \end{aligned} \tag{3.12}$$

where S_1, S_2 and S_3 are the diffusion signals corresponding to the three compartments, and f_1, f_2 and f_3 represent the volume ratio of each population.

Ball and Stick Model

Behren's ball and stick model is a simple yet useful approach for characterizing molecular diffusion as a two-compartment model [28]. The free diffusion in the extra-axonal

compartment is assumed to be an isotropic Gaussian ("the ball"), while the unidirectional diffusion within the axon, i.e., in the fibre direction, is modelled with a Gaussian for which the tensor has a single non-zero eigenvalue ("the stick").

The isotropic extra-axonal component is described by the normalized DTI signal (see Equation 3.4)

$$S_1 = e^{-b\mathbf{u}^T\mathbf{D}\mathbf{u}},$$

with the tensor $\mathbf{D} = d\mathbf{I}$, d denoting the mean diffusivity and $\mathbf{I}$ the identity tensor. The signal for the stick can be mathematically formulated as follows

$$S_2 = e^{-bd(\mathbf{n}\cdot\mathbf{u})^2},$$

where b is the b-value in equation (2.3) and $\mathbf{u}$ denotes the orientation of the diffusion gradient. The fibre direction, $\mathbf{n}$, and d are the model parameters to be estimated. Finally, equation (3.12) becomes

$$S = fS_1 + (1-f)S_2. \tag{3.13}$$

Acquisition Requirements

The data acquisition requirements for the ball and stick model are not particularly stringent; the original experiment was conducted using a single-shell sampling scheme with 60 DWIs acquired at a b-value of 1000 s/mm^2. The total scan time was 15 minutes [28].

Composite Hindered and Restricted Model of Diffusion

The Composite Hindered and Restricted Model of Diffusion proposed by Assaf et al. [43], better known as CHARMED, is another two-compartment model representing the diffusion signal as a combination of restricted diffusion in the intra-axonal space and an anisotropic Gaussian depicting hindered diffusion in the extra-axonal space. The restricted diffusion component can be further decomposed into spin populations diffusing parallel and perpendicular to the axon's axis. Displacements parallel to the fibre axis are considered to be free and hence, modelled as a 1D Gaussian which simplifies to the well-known Stejskal Tanner equation (Equation 3.4). In contrast, movement perpendicular to the axon is represented using Neuman's depiction of restricted diffusion in a cylinder. More details can be found in [44]. Formally, in this model, S is given by

$$S = f_r S_r + f_h S_h, \tag{3.14}$$

where S_r and S_h are the normalized diffusion signals from the restricted and hindered compartments, with f_r and f_h denoting the respective volume fractions.

Acquisition Requirements

The experimental design proposed by the authors for the CHARMED framework not only entails the acquisition of low angular resolution DWIs (6 directions) at low b-values, but also high angular resolution diffusion images (192 acquisitions) at b-values ranging from 2000–10,000 s/mm^2. The high angular resolution sampling is necessary for accurate estimation of the restricted diffusion profile in the intra-axonal compartments [43]. The total scan time for the dataset is around 17 minutes.

3.1.3 Metrics derived from Multi-Compartment Models

Multi-compartment models can be used to obtain geometrical features of the fibre tissue architecture, including axon density, diameter, orientation and permeability [45]. For instance, the well-known application AxCaliber, introduced by Assaf et al. extends the CHARMED framework to measure the axon diameter distribution and density [46]. The fibre diameter distributions thus obtained were comparable with those estimated using invasive histological techniques.

3.2 Non-parametric Methods

Model-based methods for depicting the diffusion process are naturally dependent on the constraints and complexity of the model employed, and hence might be unable to discern more intricate fibre configurations. For instance, in the case of fanning and bending fibre tracts, the diffusion tensor model estimates the principal direction of diffusion to be the same as in a population of parallel fibres. Additionally, it is difficult to know whether it is only the physical properties of the axonal tracts, such as the density and size, that affect the tensor shape or the actual underlying fibre structure.

Consequently, recent work has focused on evaluating the fibre orientation distribution function (fODF) from diffusion data. The methods described in this section attempt to recover the fODF either directly or by reconstructing other spherical functions that can approximate the fODF or dODF.

3.2.1 Diffusion Spectrum Imaging

As mentioned in the previous chapter, the space of all possible $\mathbf{q}$-vectors is referred to as the $\mathbf{q}$-space, giving rise to the notion of $\mathbf{q}$-space imaging (QSI) or diffusion spectrum

imaging (DSI) [47]. Three-dimensional **q**-space coverage is beneficial in its ability to discern characteristics of the diffusion behaviour that provide information about cell size, shape and transmembrane exchange [48]. Hence DSI, proposed by Wedeen et al. [49], requires dense sampling of the diffusion signal on a three-dimensional Cartesian grid at a multitude of high b-values in order to reconstruct the EAP through a numerical Fourier Transform (Equation 3.2). Often, the dODF is also computed from the EAP, enabling the approximation of the underlying fibre orientation distribution.

Acquisition Requirements

It is obvious that DSI is a significant improvement over the DTI model, allowing us to resolve crossing fibre configurations and gain further insight into complex tissue structures. However, the method remains clinically infeasible due to the prohibitively long acquisition times (typically an hour long) and large b-values required. As an example, more than 500 DWI acquisitions at b-values up to 20,000 s/mm^2 are obtained in [49] [50] to recover the EAP which is impractical in the clinical setting.

3.2.2 Q-Ball Imaging

High Angular Resolution Diffusion Imaging (HARDI), a spherical acquisition scheme developed by Tuch et al. [51] samples the **q**-space at a large number of q-vectors uniformly distributed on a spherical shell as opposed to the dense Cartesian sampling required by DSI. However, HARDI is only an acquisition protocol and must be used in conjunction with a reconstruction scheme to relate the diffusion signal to the diffusion propagator. A HARDI-based, non-parametric approach for reconstructing an unnormalised dODF using a spherical tomographic inversion, namely the Funk-Radon Transform (FRT), was advanced in [32]. The method, termed q-ball imaging (QBI) circumvents the need for dense **q**-space sampling.

The FRT of a spherical function f defined at a point $\mathbf{x}$ on the sphere can be computed as the integral of f along the arc length of the great circle $\mathbf{C}(\mathbf{x})$ comprising all unit vectors perpendicular to $\mathbf{x}$. Mathematically, the dODF can be estimated as the FRT of the diffusion signal, $E(\mathbf{q})$, on the spherical shell in **q**-space

$$\psi(\mathbf{x}) = \int_{\mathbf{q} \in C(x)} E(\mathbf{q}) d\mathbf{q}, \tag{3.15}$$

where $\mathbf{q}$ is a unit vector. It should be noted that the dODF computed in this way may suffer from blurring and low angular resolution [33].

Acquisition Requirements

The acquisition requirements of q-ball imaging are not as rigorous as DSI, with gradient directions typically ranging from 100-500, and b-values varying from 2000 to 4000 s/mm^2. However, MRI scan times still tend to be 30 minutes or higher, limiting its applicability in the clinical domain.

3.2.3 Spherical Deconvolution

Spherical deconvolution (SD) uses HARDI data to directly recover the fODF without making any prior assumptions on the underlying fibre structures. The diffusion-weighted signal attenuation emanating from a uniquely-oriented fibre population can be expressed in terms of a response function, $R(\theta)$. Here, θ is the elevation angle of the population, assuming it is aligned along the z-axis. Hence in SD, the total diffusion-weighted signal originating from a sample containing multiple distinct fibre populations is considered to be the sum of the response functions from each, weighted by their corresponding volume fractions and rotated onto their respective directions expressed in spherical coordinates (θ, ϕ) [52]. The signal is represented as

$$S(\theta, \phi) = \sum_i f_i A_i R(\theta), \tag{3.16}$$

where f_i is the volume fraction of the ith coherently-oriented fibre population, $R(\theta)$ is the aforementioned response function and A_i is the operator constituting a rotation into the orientation (θ_i, ϕ_i).

The model in Equations 3.16 and 3.17 is founded on the assumption that the order of displacement of water molecules measurable in a typical dMRI experiment is small enough for molecular exchange between orientationally-distinct fibres to be precluded. Accordingly, the diffusion-weighted signal attenuation can be represented as a convolution over the unit sphere of the fODF with the response function for a particular orientation. In particular, denoting the fODF as $f(\theta, \phi)$ in spherical coordinates, the signal can be represented as

$$S(\theta, \phi) = f(\theta, \phi) \otimes R(\theta). \tag{3.17}$$

The fODF encapsulates the volume fractions of coherently-distinct fibres. If $R(\theta)$ is known beforehand, a spherical deconvolution can then be used to extract the fODF in terms of its spherical harmonic decomposition [52].

Acquisition Requirements

In the original experiment, the authors acquired diffusion-weighted data along 60 gradient directions at a b-value of 3000 s/mm^2, allowing discrimination of fibre crossings at 40° angles and more. The total scan time was approximately 20 minutes. It is noted in [52] that results are expected to improve with increasing angular and spatial resolution and higher b-values.

3.2.4 Persistent Angular Structure (PAS) MRI

As stated previously, most dMRI methods aim to reconstruct the fibre orientation density function or its marginal distributions. Similarly, PAS MRI computes the (radially) persistent angular structure of the EAP which provides information about the movement of water molecules in each direction, and by extension about the underlying fODF [53]. The PAS can be considered to be the projection of the propagator onto a sphere of constant radius, obtained from the Fourier Transform that best fits the diffusion measurements.

In the original algorithm, Jansons and Alexander use a maximum-entropy parametrization to acquire an optimal representation of the PAS, which results in [53]

$$\tilde{p}(\hat{\mathbf{x}}) = \exp(\lambda_0 + \sum_{j=1}^{N} \lambda_j \cos(r\mathbf{q}_j \cdot \hat{\mathbf{x}})), \tag{3.18}$$

where r is the smoothness operator and the $\lambda_j, j = 0, ..., N$ are calculated using a non-linear optimization fitting procedure. Further information about the method is described in [53]. A significant benefit of the maximum-entropy representation over other linear bases is that it is positive definite and captures the spiky shapes that can better depict the white matter structure.

Acquisition Requirements

Even though the PAS function is a highly accurate characterization of the fODF compared to other dMRI methods discussed so far, it should be noted that it tends to be computationally slow. However, its acquisition requirements are relatively low, and the technique provides good performance with 54 diffusion-encoding directions and b-values in the range 1500-2000 s/mm^2 [54].

3.2.5 Mean Apparent Propagator (MAP) MRI

Since the long acquisition times involved in DSI curtail the clinical applicability of the method, a number of analytical representations of the diffusion signal that aim to compute the EAP from less arduous multi-shell acquisition sequences have recently been proposed [55] [56] [57] [58] [59]. Analytical representations of the diffusion signal are advantageous in that they tend to be more robust and their corresponding Fourier transformations also have closed form expressions. One such technique is the Mean Apparent Propagator (MAP) MRI formalism introduced by Özarslan et al. in 2013 which models the three-dimensional **q**-space signal as a weighted sum of the eigenfunctions of the simple harmonic oscillator (SHO) Hamiltonian, i.e., the Hermite polynomial basis functions [48]. The first term in the expansion is equivalent to the DTI model, where diffusion of water molecules is assumed to follow a Gaussian distribution, while higher order terms are used to represent the non-Gaussian character of anisotropic diffusion.

The aforementioned Hermite functions form a complete orthogonal basis for the space of square-integrable functions [60]. Additionally, their Fourier Transforms are also Hermite functions, enabling both the diffusion signal attenuation in 3D **q**-space and the propagator or MAP in the displacement domain to be expressed as a weighted sum of basis functions. In particular, in the rotated anatomical system, the diffusion tensor reduces to a diagonal matrix, with separable basis functions in three dimensions. Specifically,

$$A = 2\mathbf{R}^T\mathbf{D}\mathbf{R}t_d = \begin{pmatrix} u_x^2 & 0 & 0 \\ 0 & u_y^2 & 0 \\ 0 & 0 & u_z^2 \end{pmatrix}, \tag{3.19}$$

where R is the rotation matrix that diagonalizes the diffusion tensor D, and u_x, u_y and u_z are the scaling parameters given by $u_k^2 = 2\lambda_k t_d$ where t_d denotes the diffusion time and λ_k are the eigenvalues of D.

Finally, the normalized diffusion-weighted signal, $E(\mathbf{q})$ can be expressed in terms of the Hermitian polynomial basis functions, $\phi_n(\mathbf{u}, \mathbf{q})$ as

$$E(\mathbf{q}) = \sum_{n=0}^{N_{max}} \sum_{\{n_1,n_2,n_3\}} a_{n_1n_2n_3}\phi_{n_1n_2n_3}(\mathbf{A}, \mathbf{q}). \tag{3.20}$$

The diffusion propagator in the displacement domain can be expanded similarly

$$P(\mathbf{r}) = \sum_{n=0}^{N_{max}} \sum_{\{n_1,n_2,n_3\}} a_{n_1n_2n_3}\psi_{n_1n_2n_3}(\mathbf{A}, \mathbf{r}), \tag{3.21}$$

with $n_1 + n_2 + n_3 = N$ signifying the total order of the expansion, truncated at N_{max}. Since the basis functions are separable, they can be written as

$$\begin{aligned}\phi_{n_1 n_2 n_3}(\mathbf{A}, \mathbf{q}) &= \phi_{n_1}(u_x, q_x)\phi_{n_2}(u_y, q_y)\phi_{n_3}(u_z, q_z) \\ \psi_{n_1 n_2 n_3}(\mathbf{A}, \mathbf{r}) &= \psi_{n_1}(u_x, x)\psi_{n_2}(u_y, y)\psi_{n_3}(u_z, z),\end{aligned} \tag{3.22}$$

and are related through the Fourier Transform

$$\phi_n(\mathbf{u}, \mathbf{q}) = \frac{i^{-n}}{\sqrt{2^n n!}} e^{-2\pi \mathbf{q}\mathbf{u}^2} H_n(2\pi \mathbf{q}\mathbf{u}) \quad \overset{FT}{\leftrightarrow} \quad \psi_n(\mathbf{u}, \mathbf{x}) = \frac{1}{\sqrt{2^{n+1}\pi n! \mathbf{u}}} e^{\frac{-\mathbf{x}^2}{2\mathbf{u}^2}} H_n\left(\frac{\mathbf{x}}{\mathbf{u}}\right), \tag{3.23}$$

where $H_n(x)$ is the nth order Hermite polynomial. The coefficients of the expansion are calculated by solving a quadratic minimization problem once A has been estimated. For further details of the algorithm, the reader is referred to the original paper [48].

Acquisition Requirements

Although MAP MRI should ideally be able to represent any kind of signal decay and hence, more complex diffusion processes, its acquisition requirements are exacting and necessitate dense **q**-space sampling. For example, a total of 698 diffusion-weighted images were acquired on b-values ranging from 1000-6000 s/mm^2 in an acquisition time of 72 minutes in [61].

3.2.6 Derived Metrics

A variety of metrics can be derived from the diffusion measurements based on the specific diffusion model employed for signal representation. Processing HARDI data often entails computing metrics for the comparison of reconstructed ODFs across subject populations. For instance, the Kullback Leibler and Jensen-Shannon divergences have been employed for comparing different ODFs in [62] and [63]. Additionally, there has been considerable interest in formulating rotationally-invariant scalar measures for HARDI data. Özarslan et al. proposed a Generalized Anisotropy (GA) index based on the variance of diffusion coefficients and an information-theoretical parametrization of the anisotropy, termed the Scaled Entropy (SE) generalizable to higher-order tensor models and functions defined on the unit sphere [64]. Tuch introduced a mathematical framework to extract geometrical features from the spherical harmonic (SH) representation of the reconstructed ODF in [32], including a Generalized Fractional Anisotropy (GFA) index. The GFA measures the variation of the dODF. Similarly, the authors in [65] outline the use of the power spectrum

of the spherical harmonic analysis of the ODFs as a rotationally invariant diffusion measure, while [66] describes the application of SH coefficients to obtain spherical shape descriptors of the underlying functions. As the principle motivation of many dMRI schemes is the approximation of the fibre orientation distribution, many studies attempt to extract the peak shape and anisotropy corresponding to fibre tracts from the Hessian or matrix of second partial derivatives of the function [1].

3.3 Summary

Table 3.1 summarizes the parametric and non-parametric dMRI methods discussed in this chapter, along with their acquisition requirements and computation times.

Model/Method	Acquisition Requirements	Computation Time
DTI	single-shell, minimum 6 samples	low
Ball and Stick	single-shell	medium
CHARMED	single-shell, ≤ 200 samples	medium
DSI	dense Cartesian sampling	high
QBI	single-shell, $100 - 500$ samples	low/medium
SD	single-shell, ≈ 60 samples	low/medium
PAS MRI	single-shell, ≤ 60 samples	high
MAP MRI	dense multi-shell sampling	medium

Table 3.1: Comparison of Non-Parametric and Model-Based dMRI Methods

Many of the dMRI methods just described rely on high angular resolution single and multi-shell data. Such data can be characterized with complex mathematical models which are capable of shedding light on intricate sub-voxel structures, such as crossing and bending fibre geometries. For instance, some of the methods are able to compute marginal distributions of the fODF, including the dODF, allowing us to obtain information on the underlying fibre directions.

Despite this, it is apparent that a majority of the aforementioned algorithms tend to be concomitant with sophisticated dMRI acquisition protocols, relying on dense, high angular $\mathbf{q}$-space sampling. Such schemes would require significant changes to standard clinical protocols and longer acquisition times. The scan time is a singularly important feature of diffusion imaging protocols. Not only are lengthy scan times costly for hospitals, but also

it is impractical to expect patients to endure such extensive imaging. Consequently, the in-vivo data usually acquired for such diffusion studies is taken from cooperative, healthy individuals. Much work is required before current imaging hardware will be able to match the needs of the latest developments in dMRI. However, in the meantime, it would be prudent to capitalize on large imaging data repositories which have already been amassed using relatively simple, clinically-feasible diffusion protocols. Accordingly, the main focus of this research has been to develop accurate diagnostic markers from clinical dMRI protocols.

Chapter 4

Main Contribution

The main contributions of the thesis are twofold. First, we propose a conceptually novel approach for stratification of AD and NC subject groups via simultaneous analysis of multiple brain regions by drawing upon their mutual statistical associations, and second, we formulate a mathematical framework for generalizing diffusion metrics usually computed from data acquired using complex dMRI acquisition protocols (see Chapter 3) to standard, clinically-plausible acquisition schemes. We demonstrate the applicability of the technique to existing dMRI datasets, and hence, its ability to utilize diffusion data that has already been collected in the clinical setting. This chapter describes in detail the two main stages of the proposed work; a diffusion MRI pipeline developed for data preprocessing prior to image analysis and the implementation details of the proposed algorithm for discrimination between AD and NC subjects.

4.1 Diffusion Data

The data used for the purpose of this thesis was obtained from the publicly available Alzheimer's Disease Neuroimaging Initiative (ADNI) database. ADNI began in 2003 with support from the National Institute of Aging (NIA), the National Institute of Biomedical Imaging and Bioengineering (NIBIB), the Food and Drug Administration (FDA), Canadian Institutes of Health Research (CIHR), private pharmaceutical companies and various other not-for-proit corporations as a global research effort to track the progression of Alzheimer's Disease[67]. The ADNI project is a colossal effort, providing longitudinal study data taken from more than 1700 participants recruited over 50 sites across North America, who are either cognitively normal, implicated with Mild Cognitive Impairment or diagnosed with

Alzheimer's Disease. Participants are made to undergo MRI and PET scans periodically, at the first screening visit (baseline), after 3 months, 6 months, and annually thereafter over the course of a few years. The overarching goal of the ADNI study has been to combine clinical, neuroimaging, genetic, and biospecimen data for the development of diagnostic biomarkers to assess the brain's structure over the course of the disease.

A portion of the imaging data available in the ADNI database was utilized for the evaluation of the proposed algorithm. A total of 40 age-matched subjects were selected in the age range of 60-80, 20 of which were cognitively normal (10 males, 10 females) and 20 with AD. The primary motivation for using the ADNI database was to highlight the usefulness of existing dMRI data for the development of diagnostic markers for Alzheimer's Disease. The MRI data used for the study was acquired on a 3 Tesla GE Medical Systems Signa HDxt scanner, and consisted of the following images:

1. Diffusion-weighted magnetic resonance images. These were obtained using a spin echo pulse sequence (256×256 matrix; voxel size: $2.7 \times 1.37 \times 1.37$ mm^3; TR = 12,500 ms; TE = 68.4 ms; flip angle = 90°). Each DTI scan comprised a total of 46 images: 5 T2-weighted images with no diffusion sensitization ($B_{0_1} \ \ldots \ B_{0_5}$) and 41 diffusion-weighted images (DWIs) acquired with a b-value of 1000 s/mm^2 [68].

2. T1-weighted magnetic resonance images. The T1-weighted images were obtained with a high signal-to-noise ratio (SNR) Spoiled Gradient Echo (SPGR) protocol (256×256 matrix; voxel size = $1.2 \times 1.0 \times 1.0$ mm^3; TR = 6.98 ms; TE = 2.85 ms; flip angle = 11°) [68] [69].

3. T2-weighted magnetic resonance images. The T2-weighted images were acquired using a gradient echo sequence (256×256 matrix; voxel size = $4.0 \times 0.78 \times 0.78$ mm^3; TR = 650 ms; TE = 20 ms; flip angle = 20°).

4.2 Diffusion MRI Pipeline

Data preprocessing is a crucial stage for dMRI-based image analysis involving multiple data manipulation routines intended for motion artifact and eddy current correction, removal of non-cerebral tissue via skull stripping methods and automated brain labeling for brain segmentation. Identifying and removing outliers, along with compensating for misalignments between images ensures as little error as possible will be carried forward to the later stages. The significance and implementation of each stage of the diffusion MRI pipeline is described below.

Head Motion and Eddy Current Correction

It is difficult for ADNI study participants to remain completely motionless for the duration of the T1, T2 and diffusion-weighted imaging procedure, oftentimes resulting in misalignment between scans corresponding to the same subject. Cardiac pulsation may also be a source of undesirable motion in the scans. Additionally, the long diffusion gradients employed in DW MRI pulse sequences may cause a warping or stretching of diffusion images along the phase-encoding direction due to the presence of eddy currents. Hence, there is a need to compensate for the misalignment and warping caused by the aforementioned effects which can be achieved by registering diffusion-weighted images to non-diffusion-weighted ones [70].

1. The first step was affine registration with 12 Degrees of Freedom (DOF) and a least squares cost function of the non-diffusion weighted images $B_{0_2} \ldots B_{0_5}$ to the first, i.e., the B_{0_1}. This was accomplished using FMRIB (FSL) software library's FMRIB's Linear Image Registration Tool (`FLIRT`) [1]. The resulting registered images were then averaged to generate a final SNR-enhanced B_0 image using FSL's `fslmaths` tool which allows the mathematical manipulation of images.

2. Next, each of the 41 diffusion-weighted images was registered using affine transformations to the B_0 generated in the preceding step using FSL's `FLIRT` tool with 12 DOF and a correlation ratio cost function. The diffusion-encoding gradients corresponding to each DWI were also updated through rotation, according to the transformation matrices produced during the initial registration process.

Automatic Brain Segmentation

To enable the extraction of multiple brain regions, we used the `Freesurfer` Software Suite [2], a well-known open-source automatic brain segmentation tool [71] [72] [73] [74] [75] developed by the Athinoula A. Martinos Center for Biomedical Imaging at Massachusetts General Hospital to assign labels to different cortical and subcortical structures of the brain. `Freesurfer` requires the T1-weighted scan of the subject as input in addition to an optional brain mask which is used to keep only voxels that correspond to cerebral tissue and neglect voxels that are not part of brain tissue (e.g., the skull and nasal cavities). If

[1] More details regarding the tools available in the FSL library can be found at http://fsl.fmrib.ox.ac.uk/fsl/fslwiki/

[2] Implementation details can be found at https://surfer.nmr.mgh.harvard.edu/

not provided with a brain mask, the `Freesurfer` software uses the watershed segmentation algorithm to fit a spherical surface to the brain and produce its own mask [75]. However, we found that segmentation improved considerably when we employed a more rigorous procedure to generate the brain mask. Specifically, we adopted a method used by Harvard Medical School Psychiatry Neuroimaging Laboratory's (PNL) Injury and Traumatic Stress (INTRuST) unit in their publicly available diffusion and structural MRI processing pipeline [3]. The masking script used by PNL computes a number of registrations of the T1-weighted scan to a set of training images along with a weight metric measuring image similarity of each. Subsequently, it warps and adds the weighted maps together to procure the brain mask.

Before segmenting and parcellating the brain volume, `Freesurfer` first brings the data into *Talairach space* via affine registrations with the standard MNI305 template. The final outputs generated by `Freesurfer` are a number of labelled volumes, each corresponding to a different brain structure. An example of a `Freesurfer` output volume of particular interest to us is depicted in Figure 4.1.

[3]The INTRuST pipeline is publicly available at https://github.com/pnlbwh/pnlutil

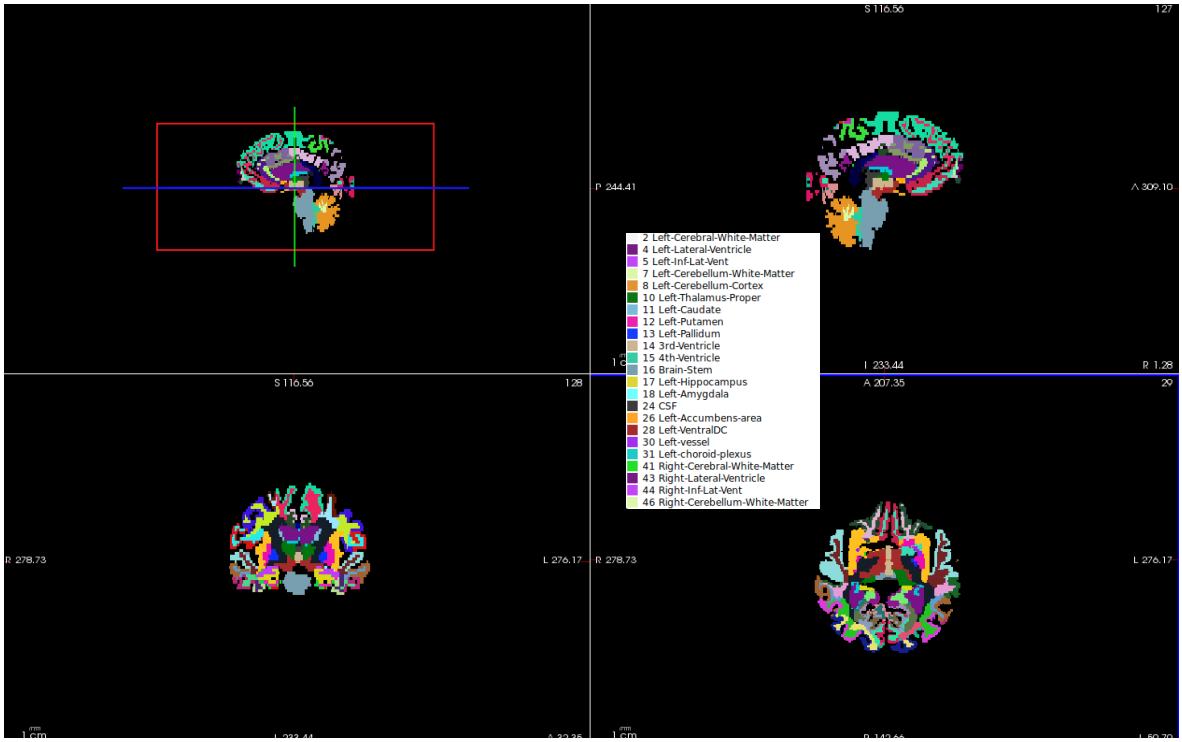

Figure 4.1: The sagittal, axial and coronal views (in clockwise order) of the parcellated white matter volume output by `Freesurfer`. The legend (white insert) depicts the `Freesurfer` labels corresponding to different white matter regions in the brain.

Transforming Freesurfer Labels to Diffusion Space

The labelled volumes extracted from a subject's structural scan by `Freesurfer` are computed in the aforementioned Talairach space. Before various white matter regions in diffusion data could be explored, these volumes needed to be resampled to the subject's corresponding diffusion space. The Advanced Normalization Tools (ANTs) software [4], an open-source framework for linear, elastic and diffeomorphic image registration [76], was employed to bring `Freesurfer` labels into diffusion space.

The T1-weighted image in the Talairach space was registered to the associated DWI with zero diffusion-weighting, i.e., the B_0, in a two-step registration process involving the subject's T2-weighted scan. A direct registration of the T1-weighted image to B_0 is

[4]The ANTs software is publicly available at http://stnava.github.io/ANTs/

undesirable because of the substantial differences in their image resolutions and contrasts; i.e., T1-weighted scans are high resolution while diffusion images are acquired with a coarser resolution. To overcome this difficulty, we exploited the fact that the T1 and T2-weighted images have similar resolutions , while the B_0 and T2-weighted scans share very similar contrasts. Thus, the T1-weighted image was first registered to the T2-weighted image, followed by a registration of the T2-weighted scan to the B_0-weighted image. Finally, the resulting geometric warps were combined and applied to the labelled volume.

The algorithmic steps described above are summarized as follows:

1. In particular, the T1-weighted scan in the Talairach space is rigidly registered to the subject's T2-weighted image using the ANTs registration package and mutual information as the similarity metric.

2. Next, a purely rigid registration with mean squared intensity difference as the similarity metric is used to register the T2-weighted scan to the average B_0 image and bring it into diffusion space. A symmetric diffeomorphic registration technique provided by ANTs, Symmetric Image Normalization (SyN), [77] with a cross-correlation similarity metric is then used to register the B_0 to the rigidly aligned T2-weighted image with a higher weighting along the phase-encoding direction to account for eddy current distortion.

3. Finally, the aforementioned transforms are composed in the correct order (the T1 to T2 forward transform, the T2 to B_0 forward transform, and the B_0 to rigidly registered T2 reverse transform) and applied to the segmented volumes to bring them into diffusion space.

It is worth emphasizing that the aforementioned procedure constitutes a critical step in the diffusion MRI pipeline since inaccurate registration can cause labels to be "off", leading to further errors in diffusion analysis.

Skull Stripping

In order to retain relevant information from the diffusion-weighted magnetic resonance images, we made use of FSL's Brain Extraction Tool (`BET`) [78] to remove non-cerebral tissue including the skull, scalp, nasal cavities and meninges [79]. A fractional intensity threshold of 0.3 and a vertical gradient of 0.3 in the threshold were found to be the optimal `BET` parameters to skull-strip the B_0 and 41 DWIs, providing a relatively good brain

estimation. The `BET` tool was also used to produce a binary brain mask for the average B_0, with 1s representing voxels that correspond to brain tissue and 0s depicting non-brain tissue voxels.

Saving Output Images

The 41 registered, skull-stripped DWIs, the B_0, and the `Freesurfer` labels in diffusion space were concatenated and stored in lexicographical order as a three-dimensional matrix for ease of analysis, with the first 41 rows corresponding to each diffusion-weighted image, the 42nd row storing the brain mask and the 43rd corresponding to the labelled image volume. The mask was also stored as a separate 3D matrix to be used for later evaluation of the diffusion data.

Quality Control

Though the diffusion MRI pipeline aims to reduce image artifacts due to patient motion, eddy currents and other sources of error, it is naturally subject to pitfalls and errors. If not rectified immediately, these errors will be carried forward in the later stages of diffusion image analysis and will be reflected in the calculation of diffusion metrics. For this reason, a quality control (QC) procedure was applied after each intermediate step of the pipeline to identify and correct any issues. Most of our QC was done in the usual way, i.e., by manual inspection of the diffusion-weighted images on a gradient by gradient, slice by slice basis [80]. The following steps were taken for this purpose:

1. Registered images are overlaid onto the reference image and checked slice by slice to see how well-aligned they are. For instance, it can be done by ensuring the ventricles of the brain volumes line up well.

2. The skull-stripped diffusion images and the brain mask are also visualized and examined for any irregularities such as "holes" in the brain surface, and the `BET` parameters adjusted if need be.

3. A basic yet essential step to verify the final outputs of the pipeline involves extracting the labels associated with the corpus callosum, an easily identifiable white matter structure made up of highly-oriented fibres. Diffusion data corresponding to the corpus callosum has long been known to be characterized by relatively high values of FA, suggesting its usefulness as a QC measure. Hence, a diffusion tensor fit is

computed in each voxel of the ROI, followed by calculating the FA values (refer to Section 3.1.1). In particular, we expect the FA values to be distributed around 0.7 indicating a high degree of anisotropic diffusion in the corpus callosum (see Figure 4.2b). Subjects that did not meet this criteria were discarded and not used for further analysis (see Figure 4.2a).

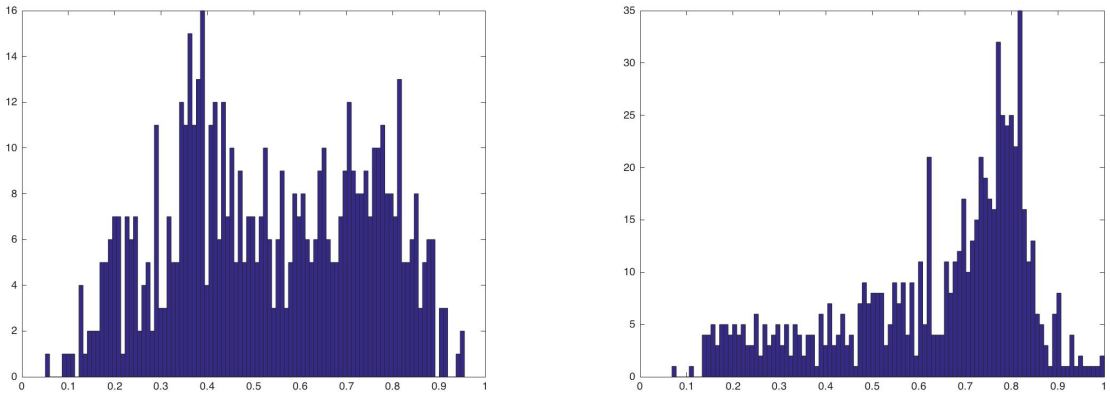

(a) FA histogram for a poorly-registered subject (b) FA histogram for a well-registered subject

4.3 Adapting Diffusion Metrics to the Spherical Shell

High angular resolution acquisitions provide access to distinctive measures of the diffusion process and the underlying tissue microstructure, for e.g., the size and shape of axonal populations not usually available from simpler indices. Such features can be extracted from the analytical representations of the full EAP. Of particular interest to us are the return-to-origin probability, propagator anisotropy and the non-gaussianity indices. Although these indices are typically computed from diffusion data acquired using complex acquisition protocols (e.g., multi-shell sampling), this section outlines how they can be adapted for the single-shell diffusion sampling while still imparting meaninful information about tissue microstructure. Before proceeding, we briefly review a meaningful basis for representation of diffusion data, i.e., the spherical harmonic (SH) transform.

Spherical Harmonic Representation of Diffusion Data

Spherical harmonics constitute a particularly useful representation and analysis for diffusion data [81]. The spherical harmonic transform is an extension of the Fourier transform to the spherical domain, and is hence well-suited for the spectral-domain representation of spherical functions [82]. Since diffusion signals are acquired over spherical shells in **q**-space, the SH transform can be used to characterize any diffusion signal acquired on the sphere. Accordingly, the spherical harmonic (SH) functions have been previously adopted for depicting the diffusion signal in each voxel as outlined in Frank [81] and Alexander et al. [83].

The spherical harmonics form a complete orthogonal basis for complex-valued functions on the three-dimensional unit sphere, $\mathbb{S}^2$. Subsequently, the normalized diffusion signal $E(\mathbf{q})$ can expressed as a linear combination of the SH functions $Y_l^m(\mathbf{q})$ such that

$$E(\mathbf{q}) = \sum_{l=0}^{\infty} \sum_{m=-l}^{l} c_l^m Y_l^m(\mathbf{q}), \tag{4.1}$$

where $\mathbf{q}$ is assumed to be a unit vector in $\mathbb{R}^3$ and c_l^m represents the series coefficient for the associated SH of order l and phase factor m. In practice, the order l is normally bounded by a maximum L based on standard considerations of sampling theory, known as the harmonic series order of the expansion. It follows that linear approximation of diffusion signals is finite in many cases, albeit approximate. For each l, there are a total of $(l+1)/2$ spherical harmonic functions affiliated with it. In spherical coordinates, the unit vector $\mathbf{q}$ can be equivalently expressed as (θ, ϕ). Thus, the diffusion signal attenuation and the SH coefficients in the spherical coordinate system can be represented as $E(\theta, \phi)$ and $Y_l^m(\theta, \phi)$ respectively, with θ corresponding to the latitude and ϕ to the longitude. $Y_l^m(\theta, \phi)$ can be expanded as

$$Y_l^m(\theta, \phi) = (-1^m)\sqrt{\frac{(2l+1)}{4\pi}\frac{(l-m)!}{(l+m)!}} P_l^m(cos\theta) e^{im\phi}, \tag{4.2}$$

where $P_l^m(x)$ are the associated Legendre polynomials given by the following equation

$$P_l^m(x) = \frac{(1-x^2)^{\frac{m}{2}}}{2^l l!}\frac{d^{l+m}}{dx^{l+m}}(x^2-1)^l. \tag{4.3}$$

The approximation power of a truncated SH expansion is determined by the maximum spherical harmonic order, L. Ideally, a large value of L would be preferable for a more

accurate characterization of diffusion signals. In practice, since diffusion signals are bandlimited, it is possible to use relatively small values of L for fitting the diffusion measurements, leading to a truncated series expansion for the diffusion signal [84]. Moreover, since $E(\mathbf{q})$ exhibits antipodal symmetry, its SH expansion involves only even-order spherical harmonics, reducing the total number of coefficients to be estimated from $(L+1)^2$ to $N = (L+1)(L+2)/2$.

In practical implementations, the number of spherical samples are finited and can be denoted by $\mathbf{u_i}, i \in \{1 \dots k\}$. In this case, Equation (4.1) can be compactly represented as a matrix vector multiplication $E = \mathcal{Y}c$ such that $\mathcal{Y} \in \mathbb{R}^{K \times N}$ is the matrix of SH functions evaluated at each of the K diffusion-encoding directions, $\mathbf{u_i} = (\theta_i, \phi_i)$, and $c \in \mathbb{R}^N$ is the vector of SH coefficients. Namely,

$$\mathcal{Y} = \begin{pmatrix} y_0^0(\mathbf{u_1}) & y_1^{-1}(\mathbf{u_1}) & y_1^0(\mathbf{u_1}) & \dots & y_L^L(\mathbf{u_1}) \\ y_0^0(\mathbf{u_2}) & y_1^{-1}(\mathbf{u_2}) & y_1^0(\mathbf{u_2}) & \dots & y_L^L(\mathbf{u_2}) \\ \vdots & \vdots & \vdots & \ddots & \vdots \\ y_0^0(\mathbf{u_K}) & y_1^{-1}(\mathbf{u_K}) & y_1^0(\mathbf{u_K}) & \dots & y_L^L(\mathbf{u_K}) \end{pmatrix}, \; c = \begin{pmatrix} c_0^0 \\ c_1^{-1} \\ c_1^0 \\ \vdots \\ c_L^L \end{pmatrix}. \tag{4.4}$$

A particularly effective way of estimating the SH coefficients for the series expansion involves a constrained least squares formulation, as proposed by Descoteaux et al. in [85]. If E denotes the column vector of diffusion measurements acquired at the $\mathbf{u_i}$s, the optimal SH coefficients can be estimated as shown

$$\underset{c}{\operatorname{argmin}} \; \|\mathcal{Y}c - E\|_2^2 + \lambda \|\Lambda c\|_2^2, \tag{4.5}$$

where $\lambda > 0$ is a user-defined regularization parameter usually equal to 0.006 [85] and $\Lambda \in \mathbb{R}^{\mathbb{N} \times \mathbb{N}}$ is the diagonal matrix representing the Laplace-Beltrami regularization, with its k^{th} diagonal entry being $l_k^2(l_k^2+1)$ while l_k corresponds to the order of the k^{th} SH coefficient. The closed form solution to Equation 4.5 is given by

$$c^* = (\mathcal{Y}^T\mathcal{Y} + \lambda\Lambda^T\Lambda)^{-1}\mathcal{Y}^T E, \tag{4.6}$$

where c^* denotes the optimal SH coefficients.

4.3.1 Return-to-Origin Probability

The return-to-origin probability, henceforth referred to as the RTOP, is the probability that a diffusing molecule undergoes zero displacement in the diffusion time Δ, i.e the time

between the two diffusion-sensitizing pulses [86] [87]. From the definition, RTOP can be deduced to be $P(\mathbf{0}, \mathbf{\Delta})$, where $P(\mathbf{x}, \mathbf{\Delta})$ is the probability distribution of a spin displacing a distance $\mathbf{x}$ in $\mathbf{\Delta}$ time (refer to Section 3.0.2). Substituting $\mathbf{x} = 0$ into Equation 3.2 provides the following expression for the RTOP

$$\begin{aligned} \text{RTOP} &= \int_{\mathbb{R}^3} e^{i2\pi \mathbf{q}\cdot\mathbf{0}} E(\mathbf{q}) d\mathbf{q} \\ &= \int_{\mathbb{R}^3} E(\mathbf{q}) d\mathbf{q}. \end{aligned} \tag{4.7}$$

Hence, the return-to-origin probability is simply the integral of the diffusion signal computed over the entire $\mathbf{q}$-space [48].

From a neurophysiological perspective, the RTOP is a measure of the restricted nature of the diffusion process. The probability is found to be higher in white matter-rich areas (e.g., the corpus callosum) than in grey matter regions like the CSF, and may be a better indicator of complex cellular structure.

Monoexponential Assumption

The diffusion data acquired using single-shell imaging is available only on a single sphere in $\mathbb{R}^3$, and hence a model is needed to characterize the behaviour of the signal over the whole sphere (i.e., inside and outside the shell). In our particular case, we use the monoexponential model which assumes the diffusion signal decays exponentially in the radial direction [33]. Specifically, at the origin, $E(\mathbf{0}) = 1$, and varies exponentially according to

$$E(\mathbf{q}) = E(q_0 \mathbf{u})^{\frac{q^2}{q_0^2}} = \tilde{E}(\mathbf{u})^{\frac{q^2}{q_0^2}}, \tag{4.8}$$

where $u \in \mathbb{S}^2$, q_0 is the radius of the spherical shell over which data is acquired, and $E(q\mathbf{u}) = e^{-\tau q^2 \cdot ADC}$. The monoexponential model is analogous to the Stejskal Tanner formalism (refer to equation (2.4)) [21] and is the same assumption made in the DTI model which encapsulates the diffusion process with an oriented Gaussian function. Monoexponentiality is a satisfactory model for the radial profile of the signal attenuation in regions with a dominant fibre population [88], and is well-suited for the single-shell diffusion data available to us in the ADNI database.

To calculate the RTOP, we fit the monoexponential model to the diffusion measurements and compute the integral in equation (4.7) in spherical coordinates. The vector $\mathbf{q}$ can

be factored into spherical coordinates as $q\mathbf{u}$ and hence, the diffusion signal can now be represented as

$$E(\theta, \phi, q) = \tilde{E}(\theta, \phi)^{\frac{q^2}{q_0^2}}. \tag{4.9}$$

Using the above monoexponential model, RTOP can be evaluated using the following integral

$$\text{RTOP} = \int_0^{2\pi}\int_0^{\pi}\int_0^{\infty} \tilde{E}(\theta, \phi)^{\frac{q^2}{q_0^2}} q^2 \sin\theta \, dq \, d\theta \, d\phi. \tag{4.10}$$

Using the substitution $y = \dfrac{q}{q_0}$ and integrating with respect to q, the equation reduces to

$$\begin{aligned} \text{RTOP} &= \int_0^{2\pi}\int_0^{\pi} \frac{\sqrt{\pi}}{4(\tau ADC(\theta, \phi))^{\frac{3}{2}}} \, d\theta \, d\phi \\ &= k \int_{\mathbb{S}^2} \frac{1}{ADC(\mathbf{u})^{\frac{3}{2}}}, \end{aligned} \tag{4.11}$$

where $k = \dfrac{\sqrt{\pi}}{4\tau^{\frac{3}{2}}}$. Thus, the computation of RTOP is reduced to evaluating a spherical integral over $\mathbb{S}^2$ which can be evaluated using the Lebedev quadrature method [89]. In particular, the Lebedev approximation for equation (4.11) works out to be

$$\text{RTOP} \simeq 4\pi k \sum_{i=1}^{N} w_i \frac{1}{ADC(\mathbf{u}_i)^{\frac{3}{2}}}, \tag{4.12}$$

where N denotes the number of grid points and $w_i, i \in \{1 \cdots N\}$ their corresponding weights. We use a 1202-point Lebedev angular quadrature approximation with a precision of 59 to calculate the RTOP. More details on the construction of the grid points can be found in [90].

4.3.2 Similarity Measures for Propagators

Given two EAPs, $P(\mathbf{r})$ and $Q(\mathbf{r})$ defined as functions of the displacement coordinate $\mathbf{r} \in \mathbb{R}^3$, a useful method for measuring similarity between the two is based on their inner product, i.e.,

$$\langle P(\mathbf{r}), Q(\mathbf{r}) \rangle = \int P(\mathbf{r}) Q(\mathbf{r}) d\mathbf{r}. \tag{4.13}$$

Using the definition of the inner product, an angular metric can be devised to gauge the similarity between the propagators

$$\cos\theta_{PQ} = \frac{\langle P(\mathbf{r}), Q(\mathbf{r})\rangle}{(\langle P(\mathbf{r}), P(\mathbf{r})\rangle\langle Q(\mathbf{r}), Q(\mathbf{r})\rangle)^{\frac{1}{2}}}. \tag{4.14}$$

This is analogous to the dot product, and hence provides information on the angular similarity of the diffusion displacement profiles. It is pertinent to note that this quantity can be evaluated in the **q**-space as well. This is a consequence of the Parseval and Plancherel theorems, which underscore the unitarity property of the Fourier transform. The Parseval theorem states that the sum of the squares of the Fourier coefficients of a function is equivalent to the integral of the square of the function. Namely,

$$\sum_{n=-\infty}^{\infty} |a_n|^2 = \frac{1}{2\pi}\int_{-\pi}^{\pi} |f(x)|^2 dx, \tag{4.15}$$

where a_n are the Fourier coefficients of f. In its most general form, this can be expressed as

$$\sum_{n=-\infty}^{\infty} a_n b_n = \frac{1}{2\pi}\int_{-\pi}^{\pi} f(x)g(x)dx, \tag{4.16}$$

with $\hat{f}(\xi)$ denoting the FT of the function.

It follows that the inner product of two vectors is preserved under orthogonal transformations. Thus, denoting the diffusion signals corresponding to the propagators as $E(\mathbf{q})$ and $F(\mathbf{q})$ respectively, we can express Equation 4.14 as

$$\cos\theta_{PQ} = \cos\theta_{EF}. \tag{4.17}$$

To make the similarity measure more intuitive for our specific application, it can be converted into a dissimilarity metric by computing $\sin\theta_{EF} = \sqrt{1-\cos\theta_{EF}^2}$. This ensures that identical propagators have zero distance, making it a true metric.

Non-Gaussianity

The non-Gaussianity (NG) metric quantifies the deviation of the diffusion signal from the Gaussian approximation of employed in the DTI model. The concept of the similarity metric can be extended to evaluate the non-Gaussianity as the angular measure between the SH representations of the diffusion signal and its Gaussian counterpart (i.e., the DTI fit

of the diffusion data) based on the method outlined in Özarslan et al. [48]. In the original method, the inner products are computed by integration over the entire **q**-space. Since we do not have access to the whole space but only a subset of the data over a spherical shell in our case, we demonstrate in this thesis that it is possible to obtain a good diagnostic diffusion measure by integrating over $\mathbb{S}^2$ instead. Hence, Cartesian integration is replaced by spherical integration. The Spherical Harmonic basis functions are used to represent the diffusion signal and its Gaussian approximation, after which the angular metric is computed between them using Equations 4.14 and 4.17.

Specifically, we start by expressing the diffusion signal $E(\mathbf{q})$, and its Gaussian approximation $F(\mathbf{q})$ using a matrix vector multiplication of the form

$$\begin{aligned} E(\mathbf{q}) &= \mathcal{Y}a \\ f(\mathbf{q}) &= \mathcal{Y}b, \end{aligned} \tag{4.18}$$

where the respective SH coefficients, a and b are computed based on the least squares formulation as described in Equation 4.6. The Gaussian approximation of $E(\mathbf{q})$ is obtained by fitting the DTI model to the diffusion measurements, also with a least square estimation routine (refer to Section 3.1.1). Consequently, the resulting NG can now be evaluated as

$$\begin{aligned} \cos\theta_{EF} &= \frac{\langle a, b\rangle}{\|a\|\|b\|} \\ \sin\theta_{EF} &= \sqrt{1-\cos\theta_{EF}^2}, \end{aligned} \tag{4.19}$$

where $\langle a, b\rangle$ and $\|a\|\|b\|$ denotes the Euclidean dot product and the vector norms respectively.

Propagator Anisotropy

The applicability of anisotropy indices to the delineation of white matter tissue is well-recognized in the literature. Notably, the FA and RA indices have served as markers for tracking neurological disorders that implicate the CNS white matter. However, based as they are on the DTI model for diffusion, these indices suffer from the same limitations and are unable to characterize intricate fibrous structures. For example, the FA is found to be lower in regions with crossing fibre populations due to the averaging caused by the Gaussian assumption of diffusion in the DTI model [91] [92]. Consequently, methods for deriving anisotropy indices from high angular resolution data have recently been proposed, many of which attempt to relate the full EAP to an anisotropy measure. One such approach is

outlined in Özarslan et al.'s MAP MRI framework, where an angular similarity measure is computed between the propagator and its respective isotropic component using the MAP MRI series coefficients [48].

An approach similar to the one outlined in the previous section can be used to calculate an anisotropy index which quantifies the isotropicity of the diffusion signal. To this end, we replace the isotropic form with a spherical approximation instead, where the latter is completely described in terms of the first coefficient of the SH signal representation which is known to encapsulate the isotropicity [81]. Hence, using equation (4.14), the anisotropy index can now be evaluated as

$$\cos\theta_{EG} = \frac{\langle a, a_0 \rangle}{\|a\|\|a_0\|}, \tag{4.20}$$

with a and a_0 representing the coefficients of the SH representation for the diffusion signal and the isotropic component respectively. Thus, Equation (4.20) can be reduced to

$$\cos\theta_{EG} = \frac{a_0^0}{\|a\|}, \tag{4.21}$$

and finally, the anisotropy index can be quantified in terms of

$$\sin\theta_{EG} = \sqrt{1 - \cos\theta_{EG}^2}. \tag{4.22}$$

Although the anisotropy index ranges from 0 to 1, it is desirable to use a scaling function to accentuate the values in a certain range, thereby enhancing contrast. Accordingly, Özarslan et al. define a family of scaling functions in [48]

$$\sigma(t, \epsilon) = \frac{t^{3\epsilon}}{1 - 3t^{\epsilon} + 3t^{2\epsilon}}, \tag{4.23}$$

which require as input the quantity ϵ being scaled, i.e., $\sin\theta_{EO}$ in our case, and a parameter t to govern the range of values to be magnified. For our specific case, the value of ϵ was taken to be 0.4.

4.3.3 Rotation-Invariant Spherical Harmonic Descriptors

In [81], Frank proposes a technique for classifying the diffusion of a voxel to be either isotropic, single-fibre or multiple-fibre based on the SH expansion of diffusion data acquired through high angular resolution schemes, i.e., HARDI measurements. Specifically, it was demonstrated that

1. Isotropic diffusion is encapsulated by the first term of the SH expansion, i.e., $c_0^0 Y_0^0(\mathbf{u})$.
2. The case of single-fibre diffusion reduces to the diffusion tensor model and can be described by $\sum_{l=0,2} \sum_m c_l^m Y_l^m(\mathbf{u})$.
3. Multiple-fibre diffusion can be described by the even orders of the SH expansion up to order $L = 4$, i.e., $\sum_{l=0,2,4} \sum_m c_l^m Y_l^m(\mathbf{u})$.

To summarize, the local diffusion can be characterized by the behaviour of their SH components of even order. The energy of these components is known to be invariant to the orientation of the signals within their respective voxels. The energies of the even order components have been known to provide important structural information about the underlying tissue, and can be formally defined as

$$e_l = \frac{1}{2l+1} \sum_{m=-l}^{l} |c_l^m|^2, \quad l = 0, 2, 4 \ldots . \tag{4.24}$$

The SH descriptors thus described prove to be useful for the analysis of diffusion signals [81].

4.4 Probabilistically-Weighted Graphs for AD Diagnosis

Characterization of the diffusion signal via parametric or model-free approaches is often followed by quantitative analysis of the diffusion measures that can be extracted from them. Typically, these approaches will be either region-based or tract-based. Region-based methods involve evaluating summary statistics of measures in different regions of the brain independently. Hence, region-based methods rely on "average" diffusion characteristics which can sometimes be a misrepresentation of the underlying distributions of the parameters. Furthermore, they are unable to gauge the interconnectivity of neuronal processing elements as brain regions are investigated independent of each other.

Alternatively, tract-based approaches employ tractography algorithms to decipher brain connectivity, after which spatial statistics and quantitative changes in the anatomical tracts can be computed [93] [94]. Although these methods take neuroanatomical connections into consideration, they are limited by the accuracy of the underlying tractography algorithm which often rely on user intervention to define tracts. Furthermore, there is much variability among the tractography results available from different software packages.

The method proposed in this work seeks a compromise between the aforementioned techniques by extending region-based approaches to the simultaneous analysis of multiple brain regions. Specifically, a set of measures corresponding to multiple brain regions is extracted from single-shell diffusion data, consisting of standard DTI metrics (such as FA, MD etc.) and metrics adapted from more complex acquisition schemes (such as the NG, RTOP) to the single-shell formalism. Since the dMRI measures tend to exhibit significant correlations with each other, the feature set is projected onto a lower dimensional subspace to reduce the interdependence. The culmination of our method is the construction of an undirected, fully-connected graph with nodes corresponding to distinct brain regions and edge weights to probabilistic distances between their respective features. Finally, the characteristics that can be extracted from such a graph serve as discriminative markers to stratify the AD and NC populations with substantial margin. Details of the implementation are presented in the following sections.

4.4.1 Feature Set Extraction

We begin by extracting white matter brain regions from `Freesurfer`-segmented volumes and characterizing each with a predefined set of features. Some of the diffusion measures are conventional metrics obtained from the diffusion tensor model, while others are metrics typically associated with high angular resolution schemes that have been adapted to the single-shell (as described in Section 4.3). The diffusion measures are summarized in Table 4.1 on the next page. Metrics are computed voxel-wise for each brain region for each subject. The dimensionality of each feature set is $m \times n$ where m is the number of voxels in the brain region and n is the number of features.

Diffusion Metric	Description	Method
Fractional Anisotropy	Proportion of tensor attributed to anisotropic diffusion	Fit DTI model to diffusion data and calculate FA as in Equation 3.7.
Relative Anisotropy	A normalized standard deviation	Fit DTI model to diffusion data and calculate RA as in Equation 3.8
Mean Diffusivity	Average diffusivity	Fit DTI model to diffusion data and calculate MD as in Equation 3.6
Volume Ratio	Ratio of diffusion ellipsoidal volume to a sphere with its radius equal to trace	Fit DTI model to diffusion data and calculate VR as in Equation 3.9
Linearity	Prolateness of diffusion ellipsoid	Fit DTI model to diffusion data and calculate measure as in Equation 3.10
Planarity	Oblateness of diffusion ellipsoid	Fit DTI model to diffusion data and calculate measure as in Equation 3.11
Rotation Invariant SH Descriptors	Power spectra of SH representation of diffusion signal	Estimate SH coefficients of diffusion data and compute power spectra (Section 4.3.3)
Return-to-Origin Probability	Probability of spins with zero displacement	Estimate SH coefficients and calculate RTOP as outlined in Section 4.3.1
Propagator Anisotropy	Dissimilarity of the SH representation of the diffusion signal and its isotropic counterpart	Estimate SH coefficients of diffusion data and compute anisotropy as in Section 4.3.2
Non-Gaussianity	Deviation of diffusion signal from Gaussian distribution	Estimate SH coefficients and calculate index as outlined in Section 4.3.2

Table 4.1: A description of the feature set extracted from diffusion data. Refer to Section 3.1.1 for estimation of DTI fit of the data and Section 4.3 on computing the SH representation of the diffusion signal.

4.4.2 Reducing Feature Interdependence

Unfortunately, the diffusion metrics exhibit excessive correlation with each other. For instance, three of our metrics (i.e., the FA, RA and propagator aisotropy) are variants of anisotropy. Additionally, we found Tuch's GFA to be proportional to the propagator anisotropy metric generalized to the single-shell formalism.

The FA index can be succinctly expressed as $\frac{\text{std}(\lambda)}{\text{rms}(\lambda)}$ with λ denoting the eigenvalues of the diffusion tensor model fitted to the data. Tuch extended this concept in [32] to formulate a generalized fractional anisotropy measure, i.e., the GFA, as shown below where ψ is the dODF computed by means of the Funk-Radon Transform (FRT) of the diffusion signal in the direction of $\mathbf{u_i}$, i.e., $\psi \approx \text{FRT}(E)$. To show this, we recall that the GFA is defined as

$$\text{GFA} = \sqrt{\frac{n \sum_{i=1}^{N} (\psi(\mathbf{u_i}) - \langle\psi\rangle)^2}{(n-1) \sum_{i=1}^{N} \psi(\mathbf{u_i})^2}}, \tag{4.25}$$

where $\psi(\mathbf{u_i})$ denotes the dODF along the i^{th} diffusion-encoding direction and $\langle\psi\rangle$, the mean of the dODF, can be simplified as $= \frac{1}{n} \sum_{i=1}^{n} \psi(u_i) = \frac{1}{n}$ due to the ODFs being normalized. By expanding the square and rearranging terms, the numerator in Equation 4.25 can be simplified as shown

$$\begin{aligned} \sum_{i=1}^{n} (\psi(\mathbf{u_i}) - \langle\psi\rangle)^2 &= \sum_{i=1}^{N} \psi(\mathbf{u_i})^2 - 2 \sum_{i=1}^{N} \langle\psi\rangle + \langle\psi\rangle^2 \\ &\underset{N\to\infty}{\longrightarrow} ||\psi||_2^2 - 2\langle\psi\rangle^2 + \langle\psi\rangle^2 \\ &= ||\psi||_2^2 - \langle\psi\rangle^2. \end{aligned} \tag{4.26}$$

Similarly, the denominator in Equation 4.25 can be expressed as

$$\begin{aligned} \sum_{i=1}^{N} |\psi(\mathbf{u_i})|^2 &\underset{N\to\infty}{\longrightarrow} \alpha \int_{\mathbb{S}^2} |\psi(\mathbf{u})|^2 d\mathbf{u} \\ &= ||\psi||_2^2. \end{aligned} \tag{4.27}$$

Finally, it should be noted that there is a linear relationship between the SH coefficients of the dODF and the coefficents of the HARDI representation of the diffusion signal. Notably,

$$\begin{aligned} \text{HARDI} \rightarrow E(\mathbf{u}) &= \sum_{n,l} c_{n,l} \mathcal{Y}_{n,l} \\ \text{dODF} \rightarrow \psi(\mathbf{u}) &= \sum_{n,l} s_{n,l} \mathcal{Y}_{n,l} \end{aligned} \tag{4.28}$$

where the SH coefficients c and s are related by

$$s_{n,l} = \lambda_n c_{n,l}, \tag{4.29}$$

with λ_n denoting the eigenvalues of the FRT. Hence, it is possible to obtain an approximation of the dODF and by extension, the GFA, from the HARDI representation of the diffusion signal. In particular, the GFA can now be computed as

$$\begin{aligned} \text{GFA} &= \frac{||\psi||_2^2 - \langle\psi\rangle^2}{||\psi||_2^2} \\ &= \frac{\sum_{n,l} |\lambda_n c_{n,l}|^2 - \lambda_0 c_{0,0}^2}{\sum_{n,l} |\lambda_n c_{n,l}|^2} \\ &= 1 - \frac{c_{0,0}^2}{\sum_{n,l} |c_{n,l}|^2}, \end{aligned} \tag{4.30}$$

and the last equation follows since $\lambda_0 = 1$. The GFA is entirely dependent on the first coefficient $c_{0,0}$, and is essentially a measure of isotropicity. Thus, it is completely analogous to the anisotropy index described in Section 4.3.2. To demonstrate this relationship, a scatter plot depicting the two metrics is displayed in Figure 4.3. One can see the plot is virtually linear, implying that one of the two metrics is redundant.

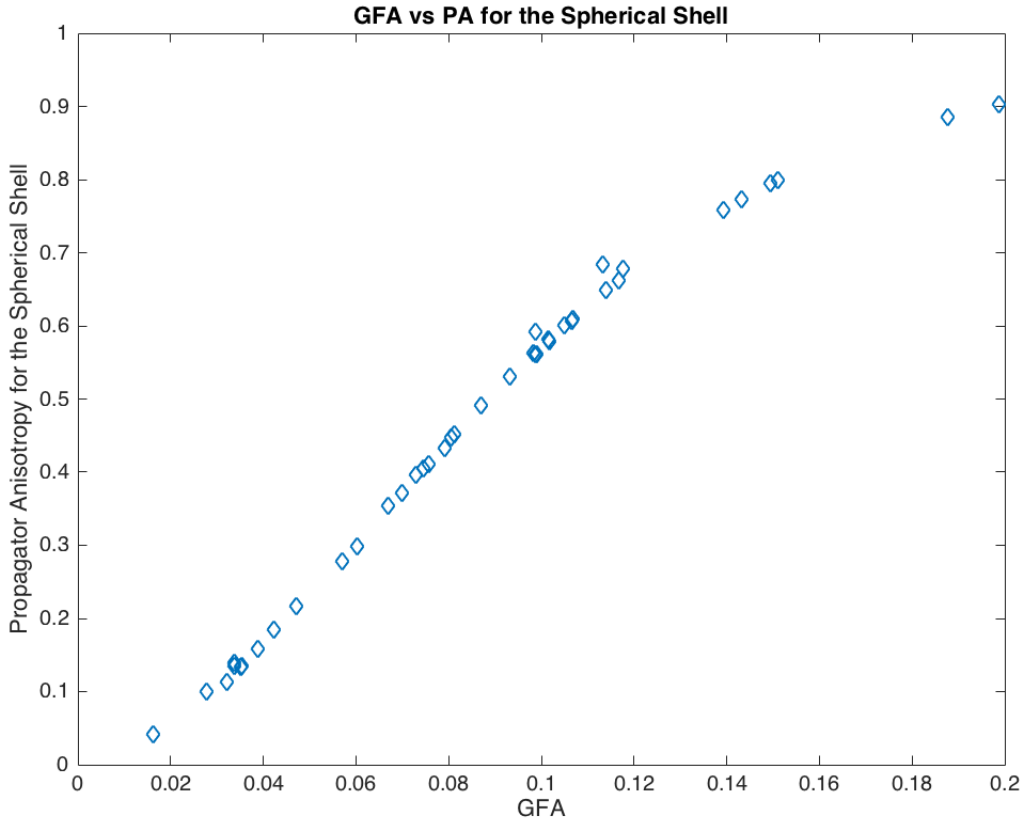

Figure 4.3: A plot depicting the virtually linear relationship between the GFA and anisotropy values.

To reduce excessive correlations within the set and retain only those features with maximum variance, a robust PCA was employed in a subject-wise fashion. In particular, the feature set for each subject was transformed to a new coordinate system to eliminate correlations between the metrics. The robust PCA implementation involved computing a robust covariance matrix using the Minimum Covariance Determinant method (FAST-MCD) [95], followed by an eigenvalue decomposition. Scree plots were used to determine the largest eigenvalues to retain. In particular, the first three features were found to have the greatest variance and were thus preserved, reducing the dimensionality of the feature set from twelve to three. Finally, the feature sets corresponding to each brain region were projected onto this new coordinate system. It should be noted that our approach focused

on utilizing second order moments of the feature set as first order moments are more susceptible to outliers. Additionally, a robust version of the PCA ensured outliers were accounted for.

4.4.3 Computing Probabilistic Distances between Brain Regions

Since AD is considered to affect multiple domains in the brain, it is particularly interesting to explore the statistical dependencies between diffusion measures corresponding to different brain regions, rather than focusing on a single region. Consequently, the next step involved computing probabilistic distances between the dimensionality-reduced feature sets within each subject.

Several choices are available for evaluating probability distance metrics. Notably, the Kullback-Leibler divergence is a widely accepted measure used to quantify the difference between two probability distributions. Given two discrete probability distributions, p and q, the KL divergence can be defined as

$$D_{KL}(p||q) = \sum_i p(i) \log \frac{p(i)}{q(i)}. \tag{4.31}$$

Assuming diffusion measures in each region follow a Gaussian distribution, the following closed-form expression can be used to compute the KL divergence for multivariate Gaussian distributions

$$D_{KL}(p||q) = \frac{1}{2}\left(\mathrm{Tr}(\Sigma_q^{-1}\Sigma_p) + (\mu_q - \mu_p)^T\Sigma_q^{-1}(\mu_q - \mu_p) - k + \ln\left(\frac{\det\Sigma_q}{\det\Sigma_p}\right)\right), \tag{4.32}$$

where μ and Σ denote the means and covariances of the distributions. Using the above equation, one can assess the probabilistic distances between any pair of empirical distributions which in our case correspond to different brain regions.

It should be noted, however, that the KL divergence is not a true metric as it is asymmetric and does not follow the triangle inequality. Hence, symmetrizing the KL divergence was given due consideration when developing the technique. We opted to use the non-negative symmetric version of the divergence as defined in [96], better known as the J-divergence. Namely,

$$\mathcal{J}(P, Q) = D_{KL}(P||Q) + D_{KL}(Q||P). \tag{4.33}$$

4.4.4 Graph Construction

A conceptually novel part of the proposed work is the use of graph-theoretical network structures to represent the probabilistic distances described in the previous section. In network theory, graphs are mathematical structures comprising a set of nodes and vertices, which are frequently employed to characterize pairwise distances between objects. Graphs are often represented as matrix structures, with rows and columns indexed by vertices, and the elements denoting pairwise distances between two vertices. As the symmetrized KL divergence is computed between each pair of brain regions, a graph representation is a suitable depiction of the probabilistic distances between the dimensionality-reduced feature sets. Accordingly, the KL divergences were used to formulate a symmetrical, graph-theoretical data matrix. As an example, computing distances between 5 different brain regions resulted in a symmetric 5×5 matrix, with zeros on the diagonal. This can be interpreted as a graph with 5 vertices or nodes corresponding to each region, with each element of the matrix denoting the probabilistic distance between them. Specifically, the following matrix depicts the pairwise probabilistic distances between the corpus callosum, parahippocampal white matter, the posterior cingulate, the cerebral white matter, and the cerebellum white matter,

$$\mathcal{J} = \begin{pmatrix} 0 & 5.02 & 11.06 & 1.88 & 8.16 \\ 5.02 & 0 & 13.81 & 2.05 & 2.29 \\ 11.06 & 13.81 & 0 & 15.58 & 5.85 \\ 1.88 & 2.05 & 15.58 & 0 & 3.60 \\ 8.16 & 2.29 & 5.85 & 3.60 & 0 \end{pmatrix}. \tag{4.34}$$

Hence, the divergence between regions 1 and 2 is $\mathcal{J}(R_1, R_2) = 5.02$ while that between regions 1 and 5 is $\mathcal{J}(R_1, R_5) = 8.16$.

4.4.5 Graph Characteristics as Discriminative Markers

The properties of the graph that depend wholly on its structure and remain invariant under isomorphisms are useful for graph characterization. The final step of the work proposed the use of these graph characteristics as discriminative markers for stratification of AD and NC populations. In particular, two of these properties were found to exhibit perfect separability between AD and NC subject groups, i.e., the closeness centrality and graph distance. Once the symmetric KL divergence matrices were computed for all subjects in our study, the closeness centrality and the graph distance were evaluated from each subject matrix as described in the following sections.

Closeness Centrality

Closeness centrality is essentially a measure of the distance of a given node to all other nodes. Specifically, the normalized average closeness centrality is computed as

$$\text{CLOC} = \frac{1}{N}\sum_{n=1}^{N}\left(\frac{N-1}{\sum_{j\neq i} d_n(i,j)}\right), \tag{4.35}$$

where N is the total number of nodes and $d(i,j)$ signifies the weight on the edge joining nodes i and j.

Graph Distance

The graph distance is simply the sum of all edge weights of the graph.

$$\text{GD} = \sum_i \sum_j d(i,j). \tag{4.36}$$

Interestingly, we found the graph distance and the eigenvalue centrality (the maximum eigenvalue of the KL divergence matrix) to exhibit one-to-one correspondence with each other.

4.5 Results

The `Freesurfer` labels corresponding to 5 distinct white matter brain regions were used for the analysis. Specifically, the following brain regions were employed: the corpus callosum, parahippocampal white matter, the posterior cingulate, the cerebral white matter (comprising the internal capsule among other regions), and the cerebellum white matter. Grey matter regions were not selected for the analysis as it is difficult to obtain connectivity information from grey matter at a b-value of 1000 s/mm^2, i.e., at relatively low b-values. The following figures demonstrate the results obtained when the proposed graph characteristics, in other words, the closeness centrality and graph distance, were applied to the AD and NC populations.

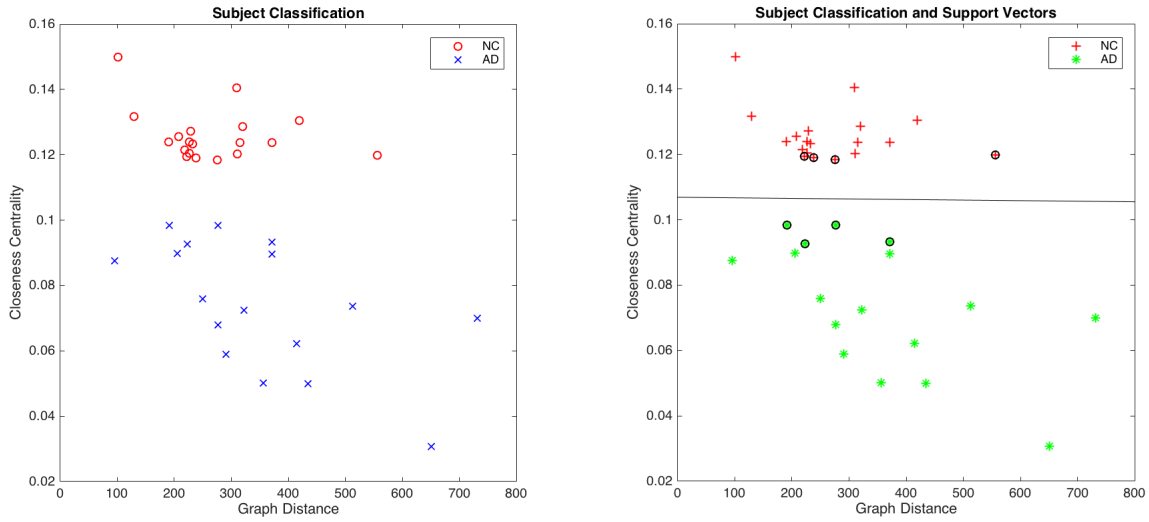

(a) (b)

Figure 4.4: (a) depicts the closeness centrality and graph distance as discriminative markers for the two subject groups, with red circles corresponding to the AD population and blue crosses denoting the NC population. (b) displays the same plot with the addition of support vectors serving as discriminative boundaries for the two subject groups

As can be seen from Figure 4.4, the characteristics derived from the connectivity matrix provide excellent separability between the two populations with no observable overlap. Additionally, a support vector machine classifier with a linear kernel was trained on the data points to find the support vectors and the optimal separating plane for the two groups. The resulting support vectors and the classification boundary are displayed alongside the data points in Figure 4.4.

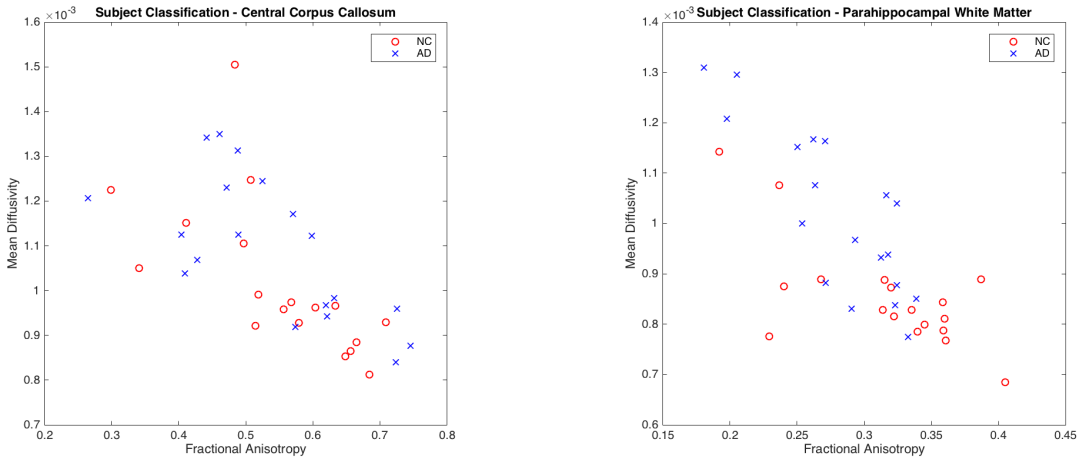

Figure 4.5: The mean FA and MD for stratification of AD and NC groups in (a) the central corpus callosum, and (b) the parahippocampal white matter. The AD subjects are represented as red circles and the NC subjects as blue crosses.

To demonstrate the merit of our proposed technique with respect to other current methods for stratification of AD and NC populations based on dMRI diagnostic markers, the average fractional anisotropy and mean diffusivity measures were evaluated from individual white matter regions and used as discriminative markers [97] [98]. Specifically, the mean FA and MD values were calculated from the corpus callosum and the parahippocampal white matter regions of the subjects and used for separating the two populations. Significant overlap was observed, as can be seen in Figure 4.5 above.

It is apparent from Figures 4.4 and 4.5 that discrimination of NC and AD subjects is a complex problem. Particularly, independent analysis of distinct brain regions using averaged diffusion measures (e.g., FA and MD) is not sufficient for separating the two groups. Not only are average statistics of diffusion measures heavily influenced by outliers, but assessing brain regions independently also limits the ability to gauge useful connectivity information. In contrast, our method offers the advantage of simultaneous analysis of multiple brain regions by exploiting statistical dependencies between them, resulting in a significant improvement in stratification of the two groups.

Chapter 5

Summary and Future Works

The results presented in this thesis lays the groundwork for the applicability of dMRI towards diagnosing neurodegenerative pathologies. In particular, we demonstrated the use of dMRI-based markers for the stratification of subjects diagnosed with Alzheimer's Disease and those who were cognitively normal. The thesis exploited the strengths of both region and tract-based approaches by proposing a conceptually-novel extension of region-based statistical methods to the simultaneous analysis of multiple brain regions. Additionally, we developed a mathematical formulation for adapting diffusion metrics typically obtained from sophisticated dMRI protocols (e.g., return-to-origin probability) to simpler, clinically-feasible protocols. These diffusion metrics, along with other standard diffusion measures were used to characterize each brain region. Next, the statistical associations between them were evaluated as probabilistic distances. The resulting connectivity pattern was modelled as an undirected, fully-connected graph with probabilistic weights. The characteristics of such graphs were shown to be excellent discriminative markers for AD and NC subjects, as verified using samples from the ADNI database.

Thus, the proposed methodology method underscored the usefulness of simple dMRI acquisition protocols for extracting useful structural information about the white matter. Furthermore, the significance of investigating brain regions altogether rather than independently of each other was also highlighted. Since many neurological disorders affect multiple domains of the brain, the joint analysis of regions holds more promise for clinical diagnosis, as was demonstrated in the results presented in this work.

Recently, MCI, which is widely regarded as a prodromal stage of AD has been the focus of clinicians and researchers alike. Subjects in the MCI stage may either develop full-blown AD, remain in their current condition or even improve. Being a transitional

phase between healthy ageing and the onset of Alzheimer's Disease, MCI is considered a critical stage for therapeutic intervention. Hence, there is a need for a stratification technique capable of handling, AD, NC and MCI subject groups. Although subjects in the prodromal stage of AD were omitted in this work, the perfect separability achieved between the two populations suggests that the technique holds enormous potential for fine-grained stratification of NC, MCI and AD subject groups. Therefore, future extensions to the thesis will involve the inclusion of MCI subjects in a longitudinal setting. Additionally, more subject cases should be incorporated to further corroborate the robustness of the method. It is hoped that accurate discrimination of these three groups would pave the way for early diagnosis of Alzheimer's Disease.

References

[1] H. Johansen-Berg and T. E. Behrens, *Diffusion MRI: from quantitative measurement to in vivo neuroanatomy*. Academic Press, 2013.

[2] S. Mori, *Introduction to diffusion tensor imaging*. Elsevier, 2007.

[3] H.-E. Assemlal, D. Tschumperlé, L. Brun, and K. Siddiqi, "Recent advances in diffusion mri modeling: Angular and radial reconstruction," *Medical image analysis*, vol. 15, no. 4, pp. 369–396, 2011.

[4] P. Mukherjee, J. Berman, S. Chung, C. Hess, and R. Henry, "Diffusion tensor mr imaging and fiber tractography: theoretic underpinnings," *American journal of neuroradiology*, vol. 29, no. 4, pp. 632–641, 2008.

[5] P. K. Spiegel, "The first clinical x-ray made in america–100 years.," *AJR. American journal of roentgenology*, vol. 164, no. 1, pp. 241–243, 1995.

[6] O. Sporns, G. Tononi, and R. Kötter, "The human connectome: a structural description of the human brain," *PLoS Comput Biol*, vol. 1, no. 4, p. e42, 2005.

[7] J. L. Prince and J. M. Links, *Medical imaging signals and systems*. Pearson Prentice Hall Upper Saddle River, NJ, 2006.

[8] B. Horwitz, K. J. Friston, and J. G. Taylor, "Neural modeling and functional brain imaging: an overview," *Neural networks*, vol. 13, no. 8, pp. 829–846, 2000.

[9] R. D. Fields, "Change in the brain's white matter," *Science*, vol. 330, no. 6005, pp. 768–769, 2010.

[10] "Canadian Mental Health Association - alzheimer's disease," 2012.

[11] H. J. Gertz and T. Arendt, *Alzheimers Disease-From Basic Research to Clinical Applications*, vol. 54. Springer Science & Business Media, 2013.

[12] A. Brun and E. Englund, "A white matter disorder in dementia of the alzheimer type: a pathoanatomical study," *Annals of neurology*, vol. 19, no. 3, pp. 253–262, 1986.

[13] H. Hanyu, T. Asano, H. Sakurai, Y. Imon, T. Iwamoto, M. Takasaki, H. Shindo, and K. Abe, "Diffusion-weighted and magnetization transfer imaging of the corpus callosum in alzheimers disease," *Journal of the neurological sciences*, vol. 167, no. 1, pp. 37–44, 1999.

[14] S. E. Rose, F. Chen, J. B. Chalk, F. O. Zelaya, W. E. Strugnell, M. Benson, J. Semple, and D. M. Doddrell, "Loss of connectivity in alzheimer's disease: an evaluation of white matter tract integrity with colour coded mr diffusion tensor imaging," *Journal of Neurology, Neurosurgery & Psychiatry*, vol. 69, no. 4, pp. 528–530, 2000.

[15] M. Rocca, M. Cercignani, G. Iannucci, G. Comi, and M. Filippi, "Weekly diffusion-weighted imaging of normal-appearing white matter in ms," *Neurology*, vol. 55, no. 6, pp. 882–884, 2000.

[16] M. Hoehn-Berlage, "Diffusion-weighted nmr imaging: application to experimental focal cerebral ischemia," *NMR in Biomedicine*, vol. 8, no. 7, pp. 345–358, 1995.

[17] K. Szabo, A. Poepel, B. Pohlmann-Eden, J. Hirsch, T. Back, O. Sedlaczek, M. Hennerici, and A. Gass, "Diffusion-weighted and perfusion mri demonstrates parenchymal changes in complex partial status epilepticus," *Brain*, vol. 128, no. 6, pp. 1369–1376, 2005.

[18] Z.-P. . Liang and P. C. Lauterbur, *Principles of magnetic resonance imaging: a signal processing perspective*. The Institute of Electrical and Electronics Engineers Press, 2000.

[19] E. L. Hahn, "Spin echoes," *Physical review*, vol. 80, no. 4, p. 580, 1950.

[20] H. Y. Carr and E. M. Purcell, "Effects of diffusion on free precession in nuclear magnetic resonance experiments," *Physical review*, vol. 94, no. 3, p. 630, 1954.

[21] E. O. Stejskal and J. E. Tanner, "Spin diffusion measurements: spin echoes in the presence of a time-dependent field gradient," *The journal of chemical physics*, vol. 42, no. 1, pp. 288–292, 1965.

[22] J. Edgar and J. Garbern, "The myelinated axon is dependent on the myelinating cell for support and maintenance: molecules involved," *Journal of neuroscience research*, vol. 76, no. 5, pp. 593–598, 2004.

[23] D. Le Bihan, "Looking into the functional architecture of the brain with diffusion mri," *Nature Reviews Neuroscience*, vol. 4, no. 6, pp. 469–480, 2003.

[24] M. Descoteaux, R. Deriche, T. R. Knösche, and A. Anwander, "Deterministic and probabilistic tractography based on complex fibre orientation distributions," *Medical Imaging, IEEE Transactions on*, vol. 28, no. 2, pp. 269–286, 2009.

[25] M. Moseley, Y. Cohen, J. Mintorovitch, L. Chileuitt, H. Shimizu, J. Kucharczyk, M. Wendland, and P. Weinstein, "Early detection of regional cerebral ischemia in cats: comparison of diffusion-and t2-weighted mri and spectroscopy," *Magnetic resonance in medicine*, vol. 14, no. 2, pp. 330–346, 1990.

[26] J. Goveas, L. ODwyer, M. Mascalchi, M. Cosottini, S. Diciotti, S. De Santis, L. Passamonti, C. Tessa, N. Toschi, and M. Giannelli, "Diffusion-mri in neurodegenerative disorders," *Magnetic resonance imaging*, vol. 33, no. 7, pp. 853–876, 2015.

[27] D. Le Bihan, J.-F. Mangin, C. Poupon, C. A. Clark, S. Pappata, N. Molko, and H. Chabriat, "Diffusion tensor imaging: concepts and applications," *Journal of magnetic resonance imaging*, vol. 13, no. 4, pp. 534–546, 2001.

[28] T. Behrens, M. Woolrich, M. Jenkinson, H. Johansen-Berg, R. Nunes, S. Clare, P. Matthews, J. Brady, and S. Smith, "Characterization and propagation of uncertainty in diffusion-weighted mr imaging," *Magnetic resonance in medicine*, vol. 50, no. 5, pp. 1077–1088, 2003.

[29] V. J. Wedeen, R. Wang, J. D. Schmahmann, T. Benner, W. Tseng, G. Dai, D. Pandya, P. Hagmann, H. D'Arceuil, and A. J. de Crespigny, "Diffusion spectrum magnetic resonance imaging (dsi) tractography of crossing fibers," *Neuroimage*, vol. 41, no. 4, pp. 1267–1277, 2008.

[30] D. K. Jones, S. C. R. Williams, D. Gasston, M. A. Horsfield, A. Simmons, and R. Howard, "Isotropic resolution diffusion tensor imaging with whole brain acquisition in a clinically acceptable time," *Human brain mapping*, vol. 15, no. 4, pp. 216–230, 2002.

[31] P. T. Callaghan, *Principles of nuclear magnetic resonance microscopy*. Oxford University Press on Demand, 1993.

[32] D. S. Tuch, "Q-ball imaging," *Magnetic resonance in medicine*, vol. 52, no. 6, pp. 1358–1372, 2004.

[33] I. Aganj, C. Lenglet, G. Sapiro, E. Yacoub, K. Ugurbil, and N. Harel, "Reconstruction of the orientation distribution function in single-and multiple-shell q-ball imaging within constant solid angle," *Magnetic Resonance in Medicine*, vol. 64, no. 2, pp. 554–566, 2010.

[34] C.-F. Westin, S. Peled, H. Gudbjartsson, R. Kikinis, F. A. Jolesz, *et al.*, "Geometrical diffusion measures for mri from tensor basis analysis," in *Proceedings of ISMRM*, vol. 97, p. 1742, 1997.

[35] A. L. Alexander, J. E. Lee, M. Lazar, and A. S. Field, "Diffusion tensor imaging of the brain," *Neurotherapeutics*, vol. 4, no. 3, pp. 316–329, 2007.

[36] P. van Gelderen, M. H. de Vleeschouwer, D. DesPres, J. Pekar, P. van Zijl, and C. T. Moonen, "Water diffusion and acute stroke," *Magnetic Resonance in Medicine*, vol. 31, no. 2, pp. 154–163, 1994.

[37] K. M. Gauvain, R. C. McKinstry, P. Mukherjee, A. Perry, J. J. Neil, B. A. Kaufman, and R. J. Hayashi, "Evaluating pediatric brain tumor cellularity with diffusion-tensor imaging," *American Journal of Roentgenology*, vol. 177, no. 2, pp. 449–454, 2001.

[38] J. J. Neil, S. I. Shiran, R. C. McKinstry, G. L. Schefft, A. Z. Snyder, C. R. Almli, E. Akbudak, J. A. Aronovitz, J. P. Miller, B. Lee, *et al.*, "Normal brain in human newborns: apparent diffusion coefficient and diffusion anisotropy measured by using diffusion tensor mr imaging.," *Radiology*, vol. 209, no. 1, pp. 57–66, 1998.

[39] G. Nicoletti, R. Lodi, F. Condino, C. Tonon, F. Fera, E. Malucelli, D. Manners, M. Zappia, L. Morgante, P. Barone, *et al.*, "Apparent diffusion coefficient measurements of the middle cerebellar peduncle differentiate the parkinson variant of msa from parkinson's disease and progressive supranuclear palsy," *Brain*, vol. 129, no. 10, pp. 2679–2687, 2006.

[40] M. F. Schocke, K. Seppi, R. Esterhammer, C. Kremser, K. J. Mair, B. V. Czermak, W. Jaschke, W. Poewe, and G. K. Wenning, "Trace of diffusion tensor differentiates the parkinson variant of multiple system atrophy and parkinson's disease," *Neuroimage*, vol. 21, no. 4, pp. 1443–1451, 2004.

[41] P.-S. Wang, H.-M. Wu, C.-P. Lin, and B.-W. Soong, "Use of diffusion tensor imaging to identify similarities and differences between cerebellar and parkinsonism forms of multiple system atrophy," *Neuroradiology*, vol. 53, no. 7, pp. 471–481, 2011.

[42] E. Panagiotaki, T. Schneider, B. Siow, M. G. Hall, M. F. Lythgoe, and D. C. Alexander, "Compartment models of the diffusion mr signal in brain white matter: a taxonomy and comparison," *Neuroimage*, vol. 59, no. 3, pp. 2241–2254, 2012.

[43] Y. Assaf and P. J. Basser, "Composite hindered and restricted model of diffusion (charmed) mr imaging of the human brain," *Neuroimage*, vol. 27, no. 1, pp. 48–58, 2005.

[44] C. Neuman, "Spin echo of spins diffusing in a bounded medium," *The Journal of Chemical Physics*, vol. 60, no. 11, pp. 4508–4511, 1974.

[45] U. Ferizi, T. Schneider, E. Panagiotaki, G. Nedjati-Gilani, H. Zhang, C. A. Wheeler-Kingshott, and D. C. Alexander, "A ranking of diffusion mri compartment models with in vivo human brain data," *Magnetic resonance in medicine*, vol. 72, no. 6, pp. 1785–1792, 2014.

[46] Y. Assaf, T. Blumenfeld-Katzir, Y. Yovel, and P. J. Basser, "Axcaliber: a method for measuring axon diameter distribution from diffusion mri," *Magnetic Resonance in Medicine*, vol. 59, no. 6, pp. 1347–1354, 2008.

[47] P. T. Callaghan, D. MacGowan, K. Packer, and F. Zelaya, "High-resolution q-space imaging in porous structures," *Journal of Magnetic Resonance (1969)*, vol. 90, no. 1, pp. 177–182, 1990.

[48] E. Özarslan, C. G. Koay, T. M. Shepherd, M. E. Komlosh, M. O. İrfanoğlu, C. Pierpaoli, and P. J. Basser, "Mean apparent propagator (map) mri: a novel diffusion imaging method for mapping tissue microstructure," *NeuroImage*, vol. 78, pp. 16–32, 2013.

[49] V. Wedeen, T. Reese, D. Tuch, M. Weigel, J. Dou, R. Weiskoff, and D. Chessler, "Mapping fiber orientation spectra in cerebral white matter with fourier-transform diffusion mri," in *Proceedings of the 8th Annual Meeting of ISMRM, Denver*, p. 82, 2000.

[50] V. J. Wedeen, P. Hagmann, W.-Y. I. Tseng, T. G. Reese, and R. M. Weisskoff, "Mapping complex tissue architecture with diffusion spectrum magnetic resonance imaging," *Magnetic resonance in medicine*, vol. 54, no. 6, pp. 1377–1386, 2005.

[51] D. S. Tuch, R. Weisskoff, J. Belliveau, and V. Wedeen, "High angular resolution diffusion imaging of the human brain," in *Proceedings of the 7th Annual Meeting of ISMRM, Philadelphia*, vol. 321, 1999.

[52] J.-D. Tournier, F. Calamante, D. G. Gadian, and A. Connelly, "Direct estimation of the fiber orientation density function from diffusion-weighted mri data using spherical deconvolution," *NeuroImage*, vol. 23, no. 3, pp. 1176–1185, 2004.

[53] K. M. Jansons and D. C. Alexander, "Persistent angular structure: new insights from diffusion magnetic resonance imaging data," *Inverse problems*, vol. 19, no. 5, p. 1031, 2003.

[54] D. C. Alexander, "Multiple-fiber reconstruction algorithms for diffusion mri," *Annals of the New York Academy of Sciences*, vol. 1064, no. 1, pp. 113–133, 2005.

[55] H.-E. Assemlal, D. Tschumperlé, and L. Brun, "Efficient and robust computation of pdf features from diffusion mr signal," *Medical image analysis*, vol. 13, no. 5, pp. 715–729, 2009.

[56] E. Ozarslan, C. Koay, T. Shepherd, S. Blackb, and P. Basser, "Simple harmonic oscillator based reconstruction and estimation for three-dimensional q-space mri," 2009.

[57] A. P. Hosseinbor, M. K. Chung, Y.-C. Wu, and A. L. Alexander, "Bessel fourier orientation reconstruction (bfor): An analytical diffusion propagator reconstruction for hybrid diffusion imaging and computation of q-space indices," *NeuroImage*, vol. 64, pp. 650–670, 2013.

[58] J. Cheng, A. Ghosh, T. Jiang, and R. Deriche, "Model-free and analytical eap reconstruction via spherical polar fourier diffusion mri," in *Medical Image Computing and Computer-Assisted Intervention–MICCAI 2010*, pp. 590–597, Springer, 2010.

[59] W. Ye, S. Portnoy, A. Entezari, S. J. Blackband, and B. C. Vemuri, "An efficient interlaced multi-shell sampling scheme for reconstruction of diffusion propagators," *Medical Imaging, IEEE Transactions on*, vol. 31, no. 5, pp. 1043–1050, 2012.

[60] H. C. Ohanian, *Principles of quantum mechanics*. Addison-Wesley, 1990.

[61] A. V. Avram, J. E. Sarlls, A. S. Barnett, E. Özarslan, C. Thomas, M. O. Irfanoglu, E. Hutchinson, C. Pierpaoli, and P. J. Basser, "Clinical feasibility of using mean apparent propagator (map) mri to characterize brain tissue microstructure," *NeuroImage*, vol. 127, pp. 422–434, 2016.

[62] M. Descoteaux and R. Deriche, "High angular resolution diffusion mri segmentation using region-based statistical surface evolution," *Journal of Mathematical Imaging and Vision*, vol. 33, no. 2, pp. 239–252, 2009.

[63] M.-C. Chiang, M. Barysheva, A. D. Lee, S. Madsen, A. D. Klunder, A. W. Toga, K. L. McMahon, G. I. De Zubicaray, M. Meredith, M. J. Wright, *et al.*, "Brain fiber architecture, genetics, and intelligence: a high angular resolution diffusion imaging (hardi) study," in *International Conference on Medical Image Computing and Computer-Assisted Intervention*, pp. 1060–1067, Springer, 2008.

[64] E. Özarslan, B. C. Vemuri, and T. H. Mareci, "Generalized scalar measures for diffusion mri using trace, variance, and entropy," *Magnetic resonance in Medicine*, vol. 53, no. 4, pp. 866–876, 2005.

[65] W. Zhan, E. A. Stein, and Y. Yang, "A rotation-invariant spherical harmonic decomposition method for mapping intravoxel multiple fiber structures," *Neuroimage*, vol. 29, no. 4, pp. 1212–1223, 2006.

[66] M. Kazhdan, T. Funkhouser, and S. Rusinkiewicz, "Rotation invariant spherical harmonic representation of 3 d shape descriptors," in *Symposium on geometry processing*, vol. 6, pp. 156–164, 2003.

[67] C. Hinrichs, V. Singh, L. Mukherjee, G. Xu, M. K. Chung, S. C. Johnson, A. D. N. Initiative, *et al.*, "Spatially augmented lpboosting for ad classification with evaluations on the adni dataset," *Neuroimage*, vol. 48, no. 1, pp. 138–149, 2009.

[68] T. M. Nir, N. Jahanshad, J. E. Villalon-Reina, A. W. Toga, C. R. Jack, M. W. Weiner, P. M. Thompson, A. D. N. I. (ADNI, *et al.*, "Effectiveness of regional dti measures in distinguishing alzheimer's disease, mci, and normal aging," *NeuroImage: Clinical*, vol. 3, pp. 180–195, 2013.

[69] C. R. Jack, M. A. Bernstein, N. C. Fox, P. Thompson, G. Alexander, D. Harvey, B. Borowski, P. J. Britson, J. L Whitwell, C. Ward, *et al.*, "The alzheimer's disease neuroimaging initiative (adni): Mri methods," *Journal of Magnetic Resonance Imaging*, vol. 27, no. 4, pp. 685–691, 2008.

[70] D. K. Jones, T. R. Knösche, and R. Turner, "White matter integrity, fiber count, and other fallacies: the do's and don'ts of diffusion mri," *Neuroimage*, vol. 73, pp. 239–254, 2013.

[71] B. Fischl, M. I. Sereno, and A. Dale, "Cortical surface-based analysis: Ii: Inflation, flattening, and a surface-based coordinate system," *NeuroImage*, vol. 9, no. 2, pp. 195 – 207, 1999.

[72] A. Dale, B. Fischl, and M. I. Sereno, "Cortical surface-based analysis: I. segmentation and surface reconstruction," *NeuroImage*, vol. 9, no. 2, pp. 179 – 194, 1999.

[73] B. Fischl, A. Liu, and A. M. Dale, "Automated manifold surgery: constructing geometrically accurate and topologically correct models of the human cerebral cortex," *IEEE Medical Imaging*, vol. 20, pp. 70–80, Jan 2001.

[74] B. Fischl, D. H. Salat, E. Busa, M. Albert, M. Dieterich, C. Haselgrove, A. Van Der Kouwe, R. Killiany, D. Kennedy, S. Klaveness, *et al.*, "Whole brain segmentation: automated labeling of neuroanatomical structures in the human brain," *Neuron*, vol. 33, no. 3, pp. 341–355, 2002.

[75] F. Ségonne, A. Dale, E. Busa, M. Glessner, D. Salat, H. Hahn, and B. Fischl, "A hybrid approach to the skull stripping problem in mri," *Neuroimage*, vol. 22, no. 3, pp. 1060–1075, 2004.

[76] B. B. Avants, N. J. Tustison, G. Song, P. A. Cook, A. Klein, and J. C. Gee, "A reproducible evaluation of ants similarity metric performance in brain image registration," *Neuroimage*, vol. 54, no. 3, pp. 2033–2044, 2011.

[77] B. B. Avants, C. L. Epstein, M. Grossman, and J. C. Gee, "Symmetric diffeomorphic image registration with cross-correlation: evaluating automated labeling of elderly and neurodegenerative brain," *Medical image analysis*, vol. 12, no. 1, pp. 26–41, 2008.

[78] S. M. Smith, "Fast robust automated brain extraction," *Human brain mapping*, vol. 17, no. 3, pp. 143–155, 2002.

[79] H. K. Hahn and H.-O. Peitgen, "The skull stripping problem in mri solved by a single 3d watershed transform," in *Medical Image Computing and Computer-Assisted Intervention–MICCAI 2000*, pp. 134–143, Springer, 2000.

[80] Z. Liu, Y. Wang, G. Gerig, S. Gouttard, R. Tao, T. Fletcher, and M. Styner, "Quality control of diffusion weighted images," in *SPIE medical imaging*, pp. 76280J–76280J, International Society for Optics and Photonics, 2010.

[81] L. R. Frank, "Characterization of anisotropy in high angular resolution diffusion-weighted mri," *Magnetic Resonance in Medicine*, vol. 47, no. 6, pp. 1083–1099, 2002.

[82] H. Groemer, *Geometric applications of Fourier series and spherical harmonics*, vol. 61. Cambridge University Press, 1996.

[83] D. Alexander, G. Barker, and S. Arridge, "Detection and modeling of non-gaussian apparent diffusion coefficient profiles in human brain data," *Magnetic Resonance in Medicine*, vol. 48, no. 2, pp. 331–340, 2002.

[84] C. P. Hess, P. Mukherjee, E. T. Han, D. Xu, and D. B. Vigneron, "Q-ball reconstruction of multimodal fiber orientations using the spherical harmonic basis," *Magnetic Resonance in Medicine*, vol. 56, no. 1, pp. 104–117, 2006.

[85] M. Descoteaux, E. Angelino, S. Fitzgibbons, and R. Deriche, "Regularized, fast, and robust analytical q-ball imaging," *Magnetic Resonance in Medicine*, vol. 58, no. 3, pp. 497–510, 2007.

[86] M. D. Hürlimann, L. M. Schwartz, and P. N. Sen, "Probability of return to the origin at short times: A probe of microstructure in porous media," *Physical Review B*, vol. 51, no. 21, p. 14936, 1995.

[87] P. P. Mitra, L. Latour, R. L. Kleinberg, and C. H. Sotak, "Pulsed-field-gradient nmr measurements of restricted diffusion and the return-to-the-origin probability," *Journal of Magnetic Resonance, Series A*, vol. 114, no. 1, pp. 47–58, 1995.

[88] E. Özarslan, T. M. Shepherd, B. C. Vemuri, S. J. Blackband, and T. H. Mareci, "Resolution of complex tissue microarchitecture using the diffusion orientation transform (dot)," *NeuroImage*, vol. 31, no. 3, pp. 1086–1103, 2006.

[89] V. I. Lebedev, "Quadratures on a sphere," *USSR Computational Mathematics and Mathematical Physics*, vol. 16, no. 2, pp. 10–24, 1976.

[90] V. Lebedev, "A quadrature formula for the sphere of 59th algebraic order of accuracy," *Russian Academy of Sciences-Doklady Mathematics-AMS Translation*, vol. 50, no. 2, pp. 283–286, 1995.

[91] C. Pierpaoli and P. J. Basser, "Toward a quantitative assessment of diffusion anisotropy," *Magnetic resonance in Medicine*, vol. 36, no. 6, pp. 893–906, 1996.

[92] D. S. Tuch, T. G. Reese, M. R. Wiegell, N. Makris, J. W. Belliveau, and V. J. Wedeen, "High angular resolution diffusion imaging reveals intravoxel white matter fiber heterogeneity," *Magnetic Resonance in Medicine*, vol. 48, no. 4, pp. 577–582, 2002.

[93] V. J. Wedeen, R. Wang, J. D. Schmahmann, T. Benner, W. Tseng, G. Dai, D. Pandya, P. Hagmann, H. D'Arceuil, and A. J. de Crespigny, "Diffusion spectrum magnetic resonance imaging (dsi) tractography of crossing fibers," *Neuroimage*, vol. 41, no. 4, pp. 1267–1277, 2008.

[94] H. Huang, J. Zhang, H. Jiang, S. Wakana, L. Poetscher, M. I. Miller, P. C. van Zijl, A. E. Hillis, R. Wytik, and S. Mori, "Dti tractography based parcellation of white matter: application to the mid-sagittal morphology of corpus callosum," *Neuroimage*, vol. 26, no. 1, pp. 195–205, 2005.

[95] P. J. Rousseeuw and K. V. Driessen, "A fast algorithm for the minimum covariance determinant estimator," *Technometrics*, vol. 41, no. 3, pp. 212–223, 1999.

[96] D. Johnson and S. Sinanovic, "Symmetrizing the kullback-leibler distance," *IEEE Transactions on Information Theory*, 2001.

[97] M. Bozzali, A. Falini, M. Franceschi, M. Cercignani, M. Zuffi, G. Scotti, G. Comi, and M. Filippi, "White matter damage in alzheimer's disease assessed in vivo using diffusion tensor magnetic resonance imaging," *Journal of Neurology, Neurosurgery & Psychiatry*, vol. 72, no. 6, pp. 742–746, 2002.

[98] M. A. Horsfield and D. K. Jones, "Applications of diffusion-weighted and diffusion tensor mri to white matter diseases–a review," *NMR in Biomedicine*, vol. 15, no. 7-8, pp. 570–577, 2002.

[99] P. J. Basser, J. Mattiello, and D. LeBihan, "Mr diffusion tensor spectroscopy and imaging.," *Biophysical journal*, vol. 66, no. 1, p. 259, 1994.